



Universidad Nacional de Colombia
Sede Bogotá
Department of Electrical and Electronics Engineering

Design and simulation of an angular space repetitive controller for an active power filter application

Sergio Andrés Dorado Rojas
Felipe Galarza Jiménez

Supervisor: Prof. Andrés Ramos Ph.D.

Submitted in part fulfilment of the requirements for the degrees of
Electrical Engineer and Electronics Engineer respectively at
Universidad Nacional de Colombia - Sede Bogotá
November 2016

Abstract

The main purpose of this document is to design an Angular Space Repetitive Control (ASRC) for an Active Power Filter (APF) in a single-phase system subjected to a nonlinear load (filtered full-wave rectifier) in order to make it robust to grid frequency deviations. A summary of the principal scientific publications referred to the topics of Repetitive Control (RC) and Angular Space Repetitive Control (ASRC) is dispensed alongside with a brief synthesis of the proposed control techniques for APFs. The paramount concepts of RC and ASRC are introduced. Posterior to this, a modelling of the plant is performed in both time-domain and angular space domain based on which the control architecture is formulated. Since the ASRC demands a constant number of samples per period, a Power-Based Phase-Locked Loop (pPLL)-based testing platform is designed and tested in a Digital Signal Processor (DSP). To conclude, simulation results on Simulink are presented for diverse frequency scenarios.

Keywords: active power filter, angular space repetitive control, grid frequency, internal model principle

Resumen

El principal objetivo de este documento es el diseño de un controlador angular repetitivo para un filtro activo de potencia en un sistema monofásico con una carga no lineal (rectificador filtrado de onda completa) de tal manera que el sistema resultante sea robusto ante desviaciones de frecuencia de la red. Se resumen las últimas publicaciones científicas referentes al tema de control repetitivo y control angular, junto a los métodos reportados para el diseño de controladores de filtros activos de potencia. En seguida, se realiza una descripción teórica de ambos conceptos, para luego proceder a un modelamiento de la planta y el planteamiento de una arquitectura de control. El concepto de control angular repetitivo requiere el diseño de una plataforma que permita tomar un número constante de muestras por período, la cual se diseña con base en un sistema de lazo cerrado Phase-Locked-Loop, cuya prueba experimental se realizó en un DSP. Los resultados de las simulaciones en Simulink se presentan para distintos escenarios de frecuencia al final del documento.

Palabras clave: control repetitivo, control repetitivo angular, filtro activo, frecuencia de la red, principio del modelo interno

Acknowledgements

We would like to express our gratitude to:

- Our supervisor Prof. Andrés Ramos Ph.D.
- Prof. Saeed Golestan, Aalborg University, Denmark.
- Prof. Sergio Raúl Rivera Rodríguez Ph.D, Universidad Nacional de Colombia.
- Prof. Jan Bacca Rodríguez Ph.D, Universidad Nacional de Colombia.
- God, our families and friends.

This project would have not been possible without your guidance and support.

The authors.

Dedication

In memory of my grandmother City,

Sergio

‘What the age needs is not a genius—it has had geniuses enough, but a martyr, who in order to teach men to obey would himself be obedient unto death. What the age needs is awakening. And therefore someday, not only my writings but my whole life, all the intriguing mystery of the machine will be studied and studied. I never forget how God helps me and it is therefore my last wish that everything may be to His honour.’

Søren Kierkegaard

Contents

Abstract	i
Acknowledgements	iii
1 Introduction	1
1.1 Motivation	1
1.2 Objectives	2
1.2.1 General Objective	2
1.2.2 Specific Objectives	2
1.3 State of the Art	2
1.4 Frequency Standards	5
2 Background Theory	6
2.1 Introduction	6
2.2 Phase-Locked Loop Systems	6
2.3 Repetitive Control	10
2.3.1 An Intuitive Approach to RC	10
2.3.2 Internal Model Principle	14

2.3.3	Periodic Signal Generator	14
2.3.4	Null-Phase FIR Filter	17
2.3.5	Plug-in Internal Model	19
2.3.6	Small-Gain Theorem	21
2.3.7	Repetitive Control Architecture	21
2.3.8	Stability Analysis	22
2.4	Angular Space Repetitive Control	26
2.4.1	Relation between Angular Space and Time Domain	26
2.4.2	Mapping into Angular Space Domain	27
2.4.3	Angular Space Transform	30
2.4.4	Space-State System Representation in Angular Space	31
2.4.5	Laplace Operator in Angular Space Domain	33
2.4.6	Z-Transform in Angular Space Domain	34
2.4.7	Angular Space Repetitive Control	34
3	Design	36
3.1	Introduction	36
3.2	Plant Modelling	38
3.2.1	Voltage Loop	42
3.2.2	Plant Precompensation	46
3.3	Design of the pPLL-based Testing Platform	49
3.3.1	Software Clock	51
3.3.2	Hardware Interruptions	53

3.4	Design of Controllers	55
3.4.1	Control Architecture	55
3.4.2	Current Loop Controller	57
3.4.3	Voltage Loop Controller	60
4	Simulation and Implementation	63
4.1	Implementation of Testing Platform	63
4.1.1	Texas Instruments F28335 Delfino	63
4.1.2	SolidThinking Embed 2016 - VisSim Embedded	64
4.2	Simulink Simulations	67
4.2.1	Dynamic pPLL Analysis	68
4.2.2	Repetitive Controller Simulation	70
4.2.3	Angular Space Repetitive Controller Simulation	72
5	Conclusion	79
5.1	Future Work	81
	Bibliography	81

List of Acronyms

APF Active Power Filter

ASRC Angular Space Repetitive Control

DFAC Double Frequency cancellation and Amplitude Compensation

DSP Digital Signal Processor

FIR Finite Impulse Response

IMP Internal Model Principle

LF Loop Filter

LPF Low-Pass Filter

LPV Linear Parameter Varying

PD Phase Detector

PLL Phase-Locked Loop

pPLL Power-Based Phase-Locked Loop

PE Power Electronics

RC Repetitive Control

VCO Voltage-Controlled Oscillator

List of Tables

4.1	Settling time of the pPLL for different combinations of frequencies.	69
4.2	Settling-time of the ASRC for the simulated frequency scenario.	72
4.3	THD variation with changes of the source voltage.	78

List of Figures

2.1	Basic PLL Structure.	7
2.2	Single-phase pPLL.	7
2.3	System in unity-feedback configuration.	10
2.4	Magnitude Bode Plot of an integrator.	12
2.5	Magnitude Bode Plot of a perfect sinusoidal generator.	13
2.6	Magnitude combined Bode Plot (cyan) of an integrator (blue) combined with two perfect sinusoidal generators (red $\rightarrow \omega = 120\pi$; green $\rightarrow \omega = 240\pi$).	13
2.7	Periodic signal generator.	15
2.8	Pole-zero map of the discrete periodic signal generator for $N = 50$	15
2.9	Bode Plot (logarithmic scale) of the periodic signal generator for $N = 50$	16
2.10	Bode Plot (linear scale) of the periodic signal generator for $N = 50$	17
2.11	Bode Plot (logarithmic scale) of a null-phase FIR filter with transfer function $0.125z^{-2} + 0.25z^{-1} + 0.5 + 0.25z + 0.125z^2$	18
2.12	Causal null-phase FIR filter.	18
2.13	Plug-in internal model.	19
2.14	Magnitude Bode Plot (logarithmic scale) of the plug-in internal model.	19
2.15	Magnitude Bode Plot (linear scale) of the plug-in internal model.	20

2.16 Pole-zero map of the plug-in internal model.	20
2.17 General positive feedback system.	21
2.18 Repetitive Control architecture.	22
2.19 Sinusoidal waveform in time domain.	26
2.20 Mapping from the time to the angular domain.	28
2.21 Frequency in the mapping from time to angular space domain.	29
2.22 Angular Space Repetitive Control architecture with plant precompensation. . . .	35
3.1 Full system	36
3.2 Single-phase shunt-connected Active Power Filter (APF).	38
3.3 Modelling of the voltage loop.	42
3.4 Angular Space Repetitive Control architecture with plant precompensation for the current loop.	46
3.5 Plant precompensation scheme.	47
3.6 Block diagram of the plant implementation scheme.	49
3.7 Implemented DFAC pPLL.	50
3.8 pPLL output	51
3.9 Modulus operation output waveform	52
3.10 Generated software clock.	52
3.11 Software clock scheme.	53
3.12 Simulation output of the software clock (in blue is shown the remainder output). .	53
3.13 Hardware Interruptions scheme.	54
3.14 Control Architecture.	55

3.15	Bode Plot of the phase-lead compensator designed for the nominal plant.	58
3.16	Magnitude bode plot of the main loop including controller and the internal model designed for the nominal plant.	58
3.17	Bode plot of the closed-loop system without ASRC ($G_o[\bar{z}]$).	59
3.18	Bode plot of the closed-loop system with ASRC.	59
3.19	Bode plot of the PI controller for the voltage loop.	61
3.20	Bode plot of the closed-loop voltage controller.	62
4.1	General system on VisSim Embedded.	64
4.2	Test system for the understanding of the interrupt signal.	65
4.3	Output of the test system with input of sinusoidal wave of 50 Hz.	65
4.4	Output of the test system with input of sinusoidal wave of 60 Hz.	66
4.5	Output of the test system with input of sinusoidal wave of 70 Hz.	66
4.6	Simulated Simulink model	67
4.7	Simulation of pPLL dynamics.	69
4.8	Currents of the system controlled by a repetitive controller design for 60 Hz with frequency changes at 0.4 and 0.7 s.	70
4.9	Tracking of the reference current by the RC current control loop.	71
4.10	THD and Power Factor of the source with a RC current control loop.	71
4.11	Currents of the system at variable-frequency scenario 65-55-60 Hz for ASRC. . .	72
4.12	Tracking of the reference current coming from the outer voltage loop by the source current	73
4.13	THD of the source and Power Factor from the source side.	73
4.14	Voltage in the DC Bus capacitor	74

4.15 Controller output 74

4.16 Tracking of a reference of 50Hz 75

4.17 THD of the source current and Power Factor from the source side. 75

4.18 Tracking of a reference of 70Hz 76

4.19 THD of the source current and Power Factor from the source side. 76

4.20 reference current and source current with variations of the voltage source amplitude 77

4.21 THD and PF of the source with variations of the voltage source amplitude . . . 77

Chapter 1

Introduction

1.1 Motivation

Climate change is one of the principal drivers for an energy transition in which the renewable energies are intended to become the main source for supplying human energetic consumption. This process will transform the actual electric grid because renewable energy sources interface with the electric grid via power electronic converters. This kind of interface lacks from the inertial capability provided by large traditional synchronous generation. Hence, the system becomes more sensitive to frequency variations due to the dynamic behaviour of the loads.

Active Power Filter (APF) is a Power Electronics (PE) device used for compensate the harmonic content of nonlinear loads with the goal of improving the power quality of the grid. In most cases, control of APFs is designed under the assumption of grid frequency will remain constant. While this might be the case for large interconnected grids, the growing of renewable energy generation makes a variable-frequency scenario even more possible.

This document aims to design a controller for a variable-frequency scenario combining the Repetitive Control (RC) technique with the angular space transform to develop the concept of Angular Space Repetitive Control (ASRC). This technique requires a special platform to generate a variable-width clock which is designed from both a software and hardware perspective.

In the end, Simulink will be used to test the control designs.

1.2 Objectives

1.2.1 General Objective

- Design and simulate an angular space repetitive controller for a single-phase shunt-connected active power filter.

1.2.2 Specific Objectives

- Assemble a simulation platform for angular space repetitive control techniques applied to power electronics systems.
- Simulate the control system for an active power filter using the designed controller.
- Analyze the behaviour of the designed controller at different frequencies.

1.3 State of the Art

A review of the related scientific literature has been carried out.

- The Internal Model Principle (IMP) [1] states that for a system in unity-feedback configuration to asymptotically track references and/or reject disturbances of a given type of signal, the signal generator (also known as *internal model*) must be included in the main control loop.
- Repetitive Control (RC) is a digital control technique based on the IMP. It is closely related to techniques such as iterative learning control and run-to-run control since all of them use past information to compute a new control signal [2]. RC has been applied in

plants subjected to periodic forcing functions such as nonlinear aerospace systems [3], disk drives [4], motors [5], heat exchangers [6] and power electronic converters [7]. The RC will be explored in Chapter 2.

- Most RC systems are designed under the assumption that the system frequency remains constant [8]. The performance of the traditional RC downgrades when the frequency of the signals is unknown or changes with time [9]. Two main approaches have been proposed to overcome this issue [8] [10]:

- *Adaptive repetitive control* which uses a variable sampling frequency by means of online adjustment of the number of samples N and/or the sampling period T_s [11].

Recall that N and T_s are related by

$$N = \frac{T_p}{T_s} \quad (1.1)$$

where T_p is the fundamental period of the reference signal.

- *High-order repetitive control* which works with a constant sampling frequency with fractional delays or interpolation in order to make the system more robust against frequency changes [10].
- Angular Space Repetitive Control (ASRC) uses a space transformation that converts the system to a domain in which the frequency can be regarded as constant, under given conditions. It has been tested on rotational motion systems required to operate at different speeds [12] [13] [14]. This topic will be further described in Chapter 2.

The Active Power Filter (APF) has been proved over the last decades to be a system capable of providing dynamic compensation on power systems [15], contributing to the improvement of power quality. The advances of power electronics and the cost evolution of self-commutating technologies as IGBTs have widen the spectrum in which control techniques have been developed for APFs.

Referring to Active Power Filter (APF) control, the methods that have been used for both three-phase and single-phase systems are noted down. The control architecture usually consists of

two loops: voltage and current loop.

It is worth to emphasize that all the following techniques were tested only at a single frequency.

For three-phase systems:

- Synchronous reference frame has been applied to develop control algorithms for the current loop with a PI controller for the voltage loop [16].
- Space Vector Modulation has been used within the current control loop [17] [18]. Genetic algorithms have been utilized for an optimized control design in which a PI compensator was used for the voltage-loop [17].
- Fuzzy logic and neuro fuzzy controllers have been designed for the current loop with testing of PI, fuzzy logic and neuro fuzzy controller for the voltage loop [19].
- Adaptive neural control control scheme has been proposed to enhance the performance of a shunt APF [20].

For single-phase systems:

- A PI controller for the voltage loop has been tested in both single-phase shunt hybrid and APFs [21].
- A direct compensation of the nonfundamental harmonics produced on the source current by a nonlinear full-wave rectifier load has been provided. In this case, the control law was based on the online computation of the cancelling harmonics to make the source current as sinusoidal as possible [22].
- A test for a PI controller for the voltage loop and an hysteresis controller for the current loop has been carried out with a nonlinear load (full-wave diode rectifier) [23].

No application of ASRC for the control of active filters has been yet reported in scientific literature.

As will be presented in the following sections, a Phased-Locked Loop (PLL) system is required to generate the interruptions needed for the spatial repetitive control to operate in a power electronics system. S. Golestan, F. Freijedo and J. Guerrero [24] proposed a double-frequency and amplitude compensation PLL for single-phase systems whose operation will be discussed in Chapter 2.

1.4 Frequency Standards

In large interconnected electric grids, the inertia of the synchronous generators does not permit huge changes in the operating frequency, in spite of the growing penetration of renewable energies which interface with the power system through power electronics converters that lack on the inertia capability of the traditional generators.

European Standard EN50160 defines the voltage characteristics of the electricity supplied by public systems. It states that the frequency deviation for microgrids operating in islanded mode shall not be greater than 15% of the nominal 50 Hz value ($\pm 7.5\text{Hz}$) [25]. This percentage is taken as reference in this work. Hence, the designed control system has to perform well within a frequency range of $50\text{ Hz} \pm 15\%$ ($\pm 7.5\text{ Hz}$).

Chapter 2

Background Theory

2.1 Introduction

In this chapter, the it is given an overview of the key concepts of Phase-Locked Loop (PLL) and Power-Based Phase-Locked Loop (pPLL), alongside with an introduction to Repetitive Control (RC) and Angular Space Repetitive Control (ASRC).

2.2 Phase-Locked Loop Systems

A Phase-Locked Loop (PLL) is a closed-loop system whose purpose is to synchronize its output signal in both frequency and phase with the fundamental component of the input signal [24].

All PLLs are composed of three parts:

- Phase Detector (PD).
- Loop Filter (LF).
- Voltage-Controlled Oscillator (VCO).

The basic structure of such systems is presented in Figure 2.1.

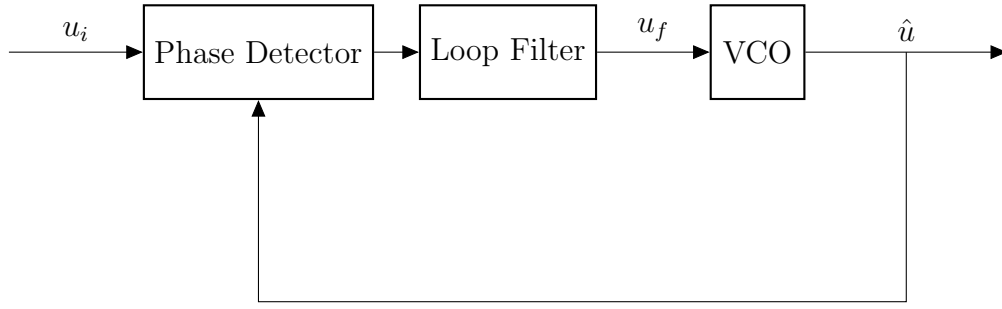


Figure 2.1: Basic PLL Structure.

In this block diagram:

- u_i : sinusoidal input voltage.
- u_f : filtered voltage.
- \hat{u} : estimated voltage.

The main difference between different PLL topologies lies in most cases in the Phase Detector stage [24] and the frequency of the input signals. The Power-Based Phase-Locked Loop (pPLL) is a PLL used for power applications such as active power filters where it plays a significant role in the estimation of the frequency and the phase angle of the connected system [24]. The single-phase pPLL configuration is presented in Figure 2.2, where the PD is composed of a sin block and a Low-Pass Filter (LPF).

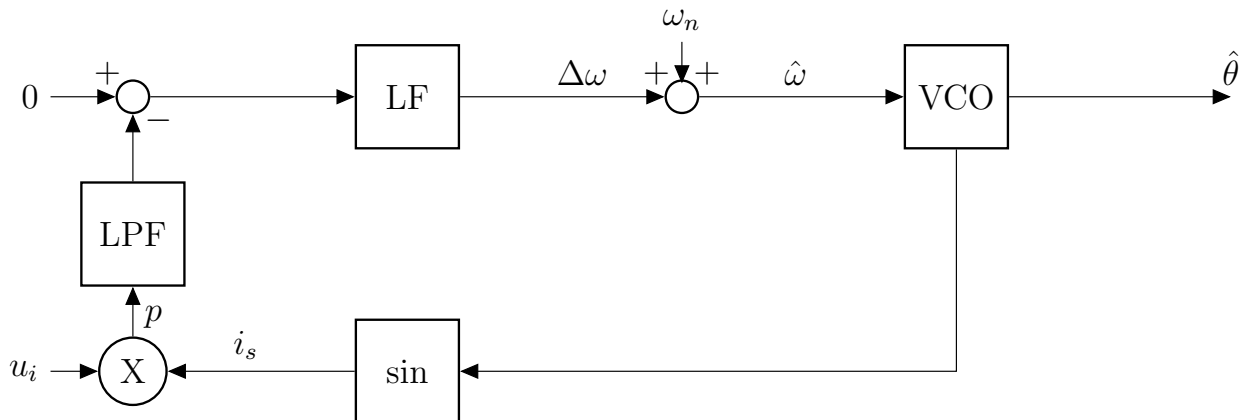


Figure 2.2: Single-phase pPLL.

In this figure:

- $\hat{\theta}$: estimated angle.

that could be written as a function of the estimated angular frequency $\hat{\omega}$ and the estimated phase angle $\hat{\phi}$:

$$\hat{\theta} = \hat{\omega}t + \hat{\phi} \quad (2.1)$$

- ω_n : nominal angular frequency of the system.

for 60 Hz networks:

$$\omega_n = 2\pi f = 2\pi(60 \text{ Hz}) = 376.9 \text{ rad/s}$$

- $\hat{\omega}$: estimated angular frequency.
- $\Delta\omega$: estimation deviation or absolute estimation error.
- i_s : fictitious current

Thereby, it can be concluded that the estimated frequency drives the VCO. If the deviation $\Delta\omega$ is zero, the output of the PD will be in phase with the voltage grid ($\theta = \hat{\theta}$ and thus $\phi = \hat{\phi}$). On the other hand, the signal p can be thought as an active power estimation. Hence the name of *fictitious current* for the output of the PD.

Let the input signal be a pure sinusoidal with peak amplitude U_p ($u_i = U_p \cos \theta$). Then, the active power estimation can be computed as:

$$p = u_i i_s = U_p \cos \theta \sin \hat{\theta} \quad (2.2)$$

By means of the product-to-sum trigonometric identity

$$\cos u \sin v = \frac{1}{2} \{ \sin(u + v) - \sin(u - v) \}$$

a more comprehensive expression for the active power estimation is obtained:

$$p = \frac{U_p}{2} \sin(\theta + \hat{\theta}) + \frac{U_p}{2} \sin(\theta - \hat{\theta}) \quad (2.3)$$

In steady-state performance, it is desired that the estimated angle $\hat{\theta}$ differs by a small amount from the grid angle θ . Thus, the angle deviation $\theta - \hat{\theta}$ is itself small and a power series approximation might be applied to equation 2.3 to obtain:

$$p = \underbrace{\frac{U_p}{2}(\theta - \hat{\theta})}_{\text{DC component}} + \underbrace{\frac{U_p}{2} \sin(\theta + \hat{\theta})}_{\text{double frequency oscillating component}} \quad (2.4)$$

As a consequence, a double frequency term of half the amplitude of the grid voltage has to be filtered out by means of a LPF in order to keep the output of the pPLL jittering within an acceptable range [24]. Consequently, the output of the loop filter after undesired signal rejection and an adequate amplitude compensation will be:

$$\Delta\omega = \theta - \hat{\theta} \quad (2.5)$$

By that means, the whole system manages to obtain an approximation for the angle θ via integration of $\Delta\omega$, accomplished by the VCO. This information can be used for designing control algorithms as will be done in the following sections.

It should be also highlighted that the voltage amplitude plays a significant role in the pPLL performance, even after the filtering stage. Since there could be several grid faults such as voltage sags which can deteriorate the estimation of the system, S. Golestan, M. Monfared, F. Freijedo and J. Guerrero [24] proposed a Double Frequency cancellation and Amplitude Compensation (DFAC) method for the PD hat successfully eliminates the double frequency component and provides system stability within changing input voltage conditions.

Whereas the description of DFAC topology is beyond the scope of this text, the reader is

encouraged to consult reference [24] to further explore this architecture. In Chapter 3, however, the dynamics of the pPLL are analyzed and in Chapter 4 experimental results of the PLL-based testing platform for spatial repetitive controllers are presented.

2.3 Repetitive Control

Repetitive Control (RC) is a discrete control technique based upon the Internal Model Principle (IMP). Since it is a discrete procedure, a discrete representation of the plant is required for designing the controller. Nonetheless, in the following section an intuitive first-approach in continuous time is to be presented in order to suitably introduce the discrete domain representation of RC.

2.3.1 An Intuitive Approach to RC

Consider a system in unity negative feedback configuration as shown in Figure 2.3 where $C(s)$ and $G(s)$ are the Laplace transforms of the controller and the plant respectively, d represents the plant input disturbances and d_o the output disturbances.

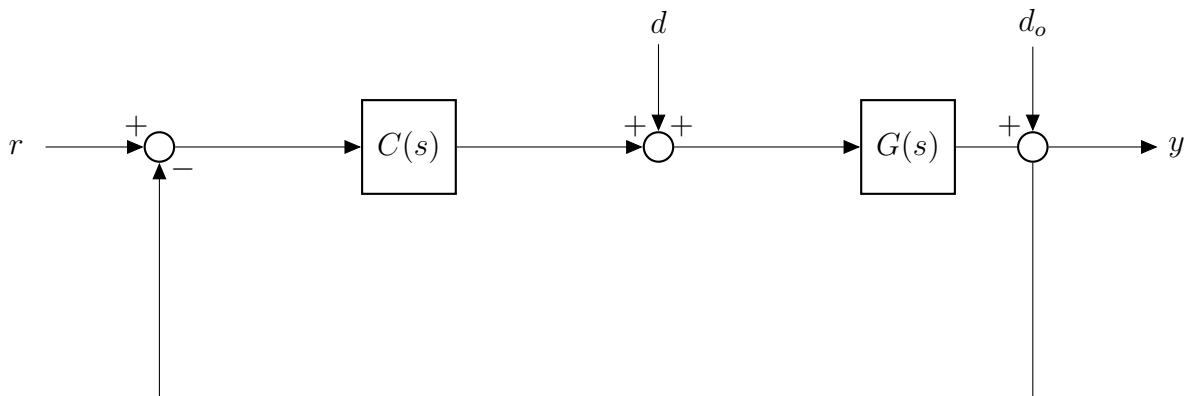


Figure 2.3: System in unity-feedback configuration.

The following transfer functions may be computed:

$$\text{Reference to output} \quad G_{ry}(s) = \frac{C(s)G(s)}{1 + C(s)G(s)} \quad (2.6)$$

$$\text{Reference to error} \quad G_{re}(s) = \frac{1}{1 + C(s)G(s)} \quad (2.7)$$

$$\text{Plant input disturbances to output} \quad G_{dy}(s) = \frac{G(s)}{1 + C(s)G(s)} \quad (2.8)$$

$$\text{Plant output disturbances to output} \quad G_{doy}(s) = \frac{1}{1 + C(s)G(s)} \quad (2.9)$$

The transfer function from reference to error is also known as *sensitivity function*. Assume the controller $C(s)$ has an infinite gain. That being so, the previous functions become:

$$\text{Reference to output} \quad G_{ry}(s) = \frac{C(s)G(s)}{1 + C(s)G(s)} \xrightarrow{C(s) \rightarrow \infty} = 1$$

$$\text{Reference to error} \quad G_{re}(s) = \frac{1}{1 + C(s)G(s)} \xrightarrow{C(s) \rightarrow \infty} = 0$$

$$\text{Plant input disturbances to output} \quad G_{dy}(s) = \frac{G(s)}{1 + C(s)G(s)} \xrightarrow{C(s) \rightarrow \infty} = 0$$

$$\text{Plant output disturbances to output} \quad G_{doy}(s) = \frac{1}{1 + C(s)G(s)} \xrightarrow{C(s) \rightarrow \infty} = 0$$

Introducing an infinite gain has made the closed-loop system capable of tracking any reference perfectly ($G_{ry} = 1$) and of rejecting the effects of the both disturbances on the output ($G_{yd} = 0$, $G_{ydo} = 0$).

Consider now a pure integral controller with transfer function $C(s) = \frac{1}{s}$ whose magnitude Bode Plot is shown in Figure 2.4. This system is capable of provide infinite gain at zero frequencies (DC). Hence, a unity-feedback control system with an integrator will be capable of following dc references and rejecting zero-frequency disturbances, although the integrator itself is a marginally stable system.

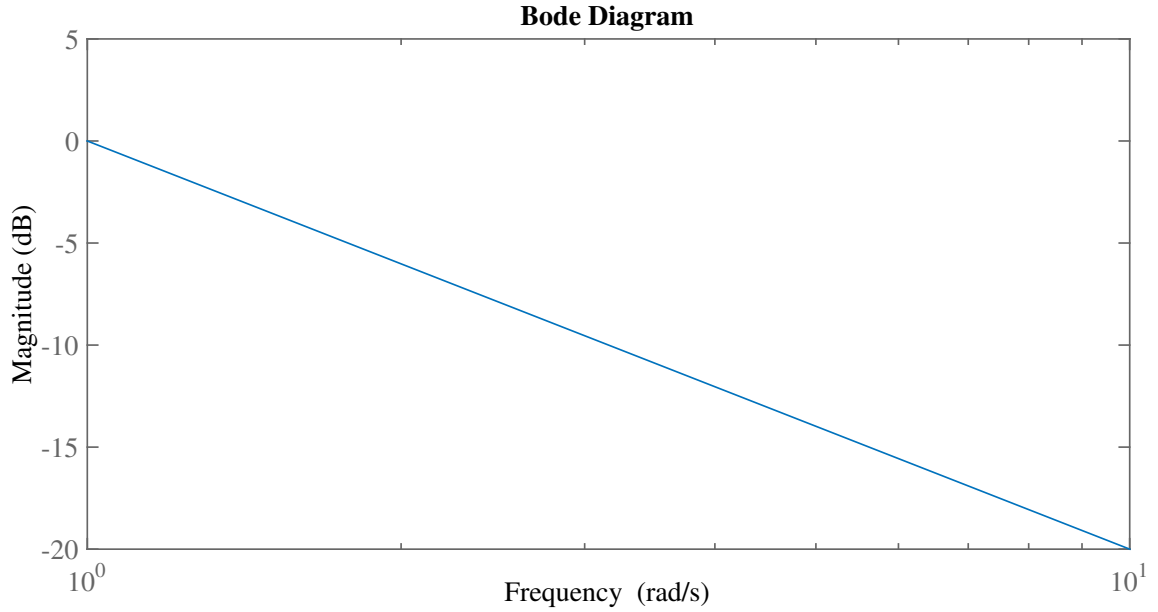


Figure 2.4: Magnitude Bode Plot of an integrator.

Another marginally stable system with imaginary poles is to be studied. This system has as a step response a sinusoidal of frequency $\omega = 120\pi$. Its corresponding Bode Plot is shown in Figure 2.5.

$$C(s) = \frac{1}{s^2 + \omega^2} = \frac{1}{s^2 + (120\pi)^2}$$

This system also introduces an infinite gain at the frequency $\omega = 120\pi$, where it is said to be in resonance. As a result, it will track sinusoidal references of the fundamental frequency $\omega = 120\pi$ asymptotically and reject sinusoidal disturbances of the same frequency.

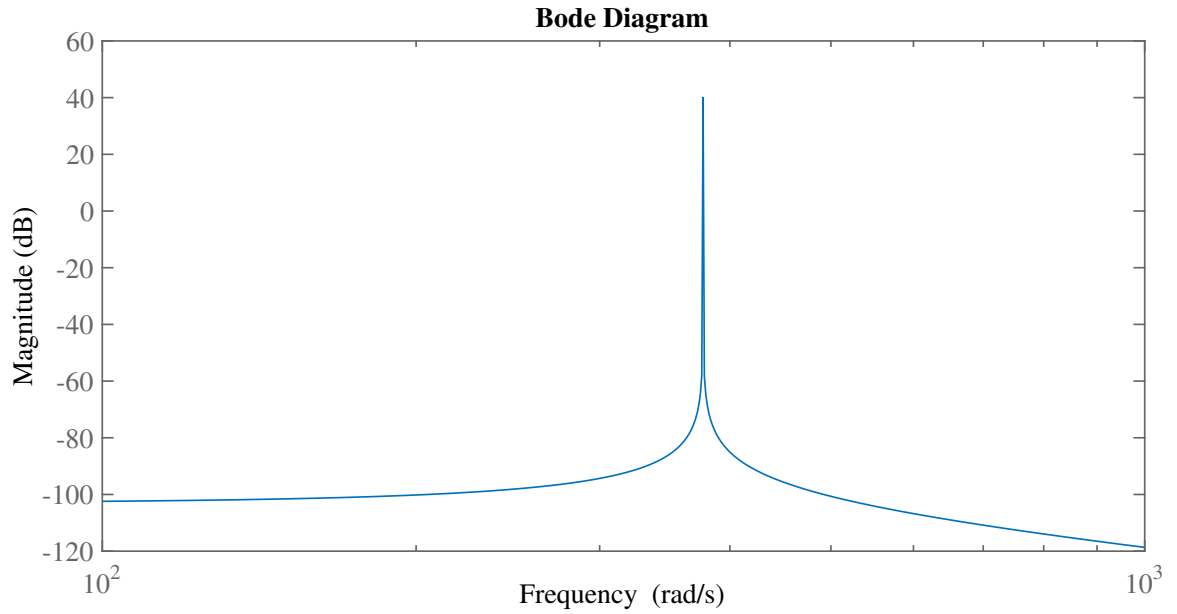


Figure 2.5: Magnitude Bode Plot of a perfect sinusoidal generator.

Multiple large gain peaks may be accomplished by cascading. The equivalent Bode Plot of such series systems is obtained graphically by adding up each of them. Figure 2.6 shows the Bode Plot of an integrator $1/s$ and two sinusoidal generators of frequencies $\omega = 120\pi$ and $\omega = 240\pi$.

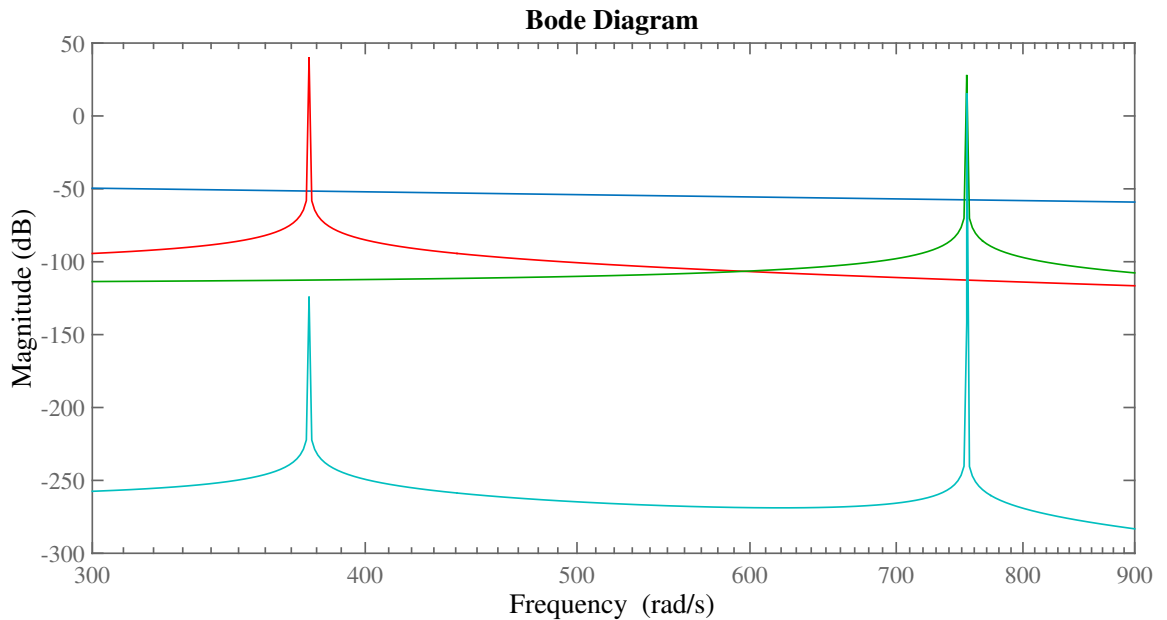


Figure 2.6: Magnitude combined Bode Plot (cyan) of an integrator (blue) combined with two perfect sinusoidal generators (red $\rightarrow \omega = 120\pi$; green $\rightarrow \omega = 240\pi$).

2.3.2 Internal Model Principle

Let $R(s)$, $D(s)$ and $D_o(s)$ be the generating polynomials of a reference signal $r(t)$, a plant input disturbance $d(t)$ and an output disturbance $d_o(t)$ respectively, which are not necessarily equal. Consider also the polynomials $P(s)$ and $Q(s)$ which do not necessarily have to correspond to the signal generators. Then, if a controller of the form

$$C(s) = \frac{P(s)}{Q(s)R(s)D(s)D_o(s)} \quad (2.10)$$

is placed in the main loop of a system in unity feedback configuration, then the system will cause the output to asymptotically track the reference and to reject the effect of the disturbances.

IMP is also related to *resonant control* and *active feedforward cancellation*. It requires the signal to be tracked or rejected to be included in the main control loop. However, it does not guarantee stability of the overall closed-loop system neither does it account for the transient performance since it is a steady-state design criteria. Therefore, the polynomials $P(s)$ and $Q(s)$ of the controller must be designed to make the system stable and to suite the given transient performance requirements.

2.3.3 Periodic Signal Generator

In power systems, it would be ideal to reject all the introduced harmonics through a nonlinear load, for example. If Internal Model Principle (IMP) is to be used for this purpose, an infinite number of sinusoidal generating polynomials have to be placed in the main control loop. Thus, a single polynomial would be required for any frequency to be rejected, yielding a very large expression to handle.

Figure 2.7 introduces a discrete time positive feedback system based on a delay principle which is capable of producing any periodic signal. For the sinusoidal case, such a configuration could be used for generating within a loop an infinite number of positive harmonics of a given frequency,

eliminating the requirement of explicitly stating the frequency of each harmonic, when IMP is to be applied. This system is called a *periodic signal generator*.

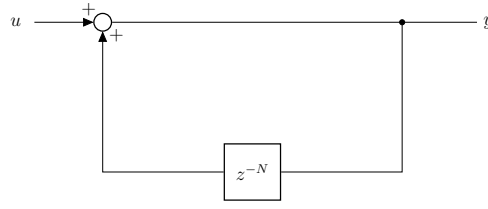


Figure 2.7: Periodic signal generator.

The transfer function of the periodic signal generator is:

$$G[z] = \frac{1}{1 - z^{-N}} = \frac{z^N}{z^N - 1} \quad (2.11)$$

The N zeros of $G[z]$ are equally distributed on the unit circle of the complex z -plane as can be detailed in Figure 2.8.

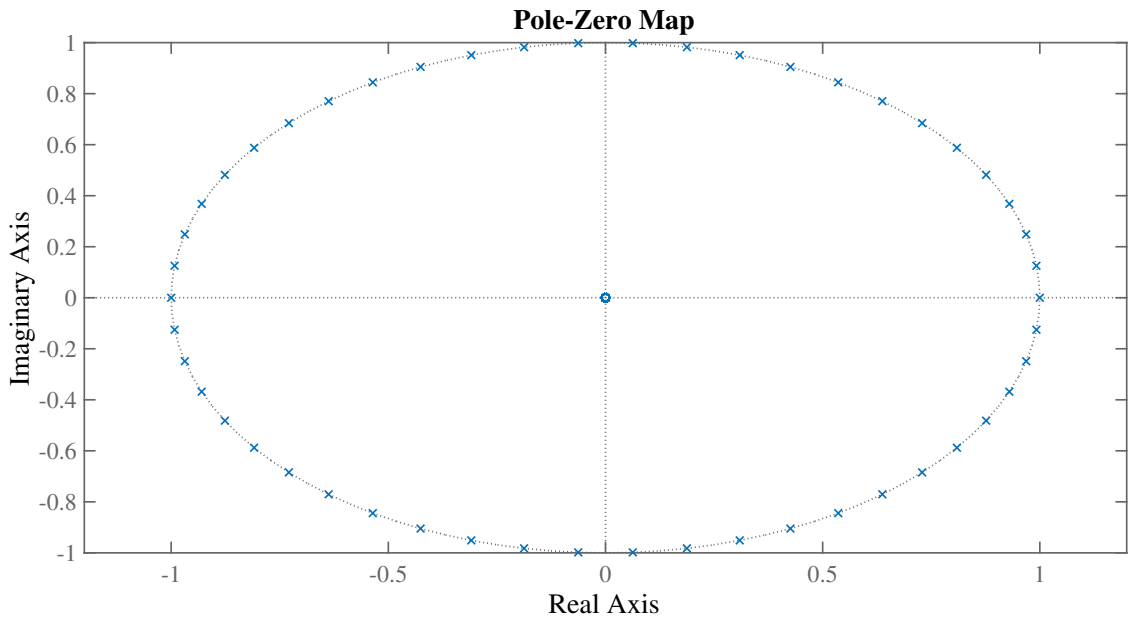


Figure 2.8: Pole-zero map of the discrete periodic signal generator for $N = 50$.

It is worth to point out that the larger the number of zeros, the greater the number of harmonics that could be rejected via IMP. As a result, N should be considerably large enough and should be computed by the formula:

$$N = \frac{T_p}{T_s} \quad (2.12)$$

where:

- T_p : periodic signal period.
- T_s : sample period.

As a final consideration, in Figure 2.9 is presented the Bode Plot of the signal generator for $N = 50$. As expected, it introduces a large gain at each of the pole frequencies which are equally spaced. Due to the logarithmic scale, this fact is not easily observable. In Figure 2.10 this Bode Plot is found in linear scale where the equal placement of the resonance peaks is clearer.

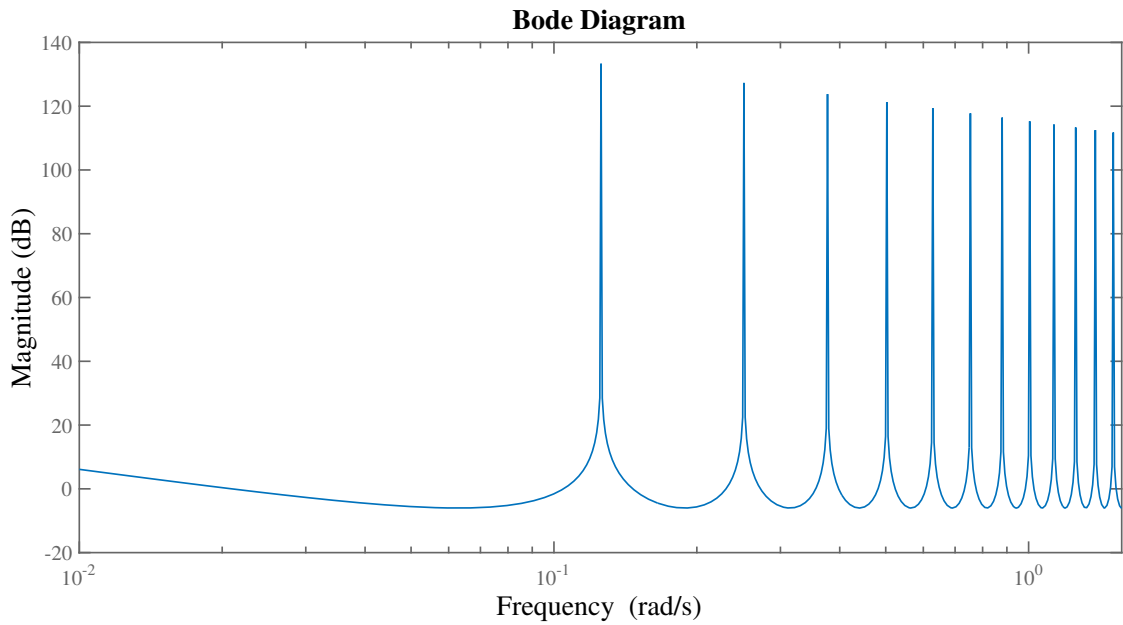


Figure 2.9: Bode Plot (logarithmic scale) of the periodic signal generator for $N = 50$.

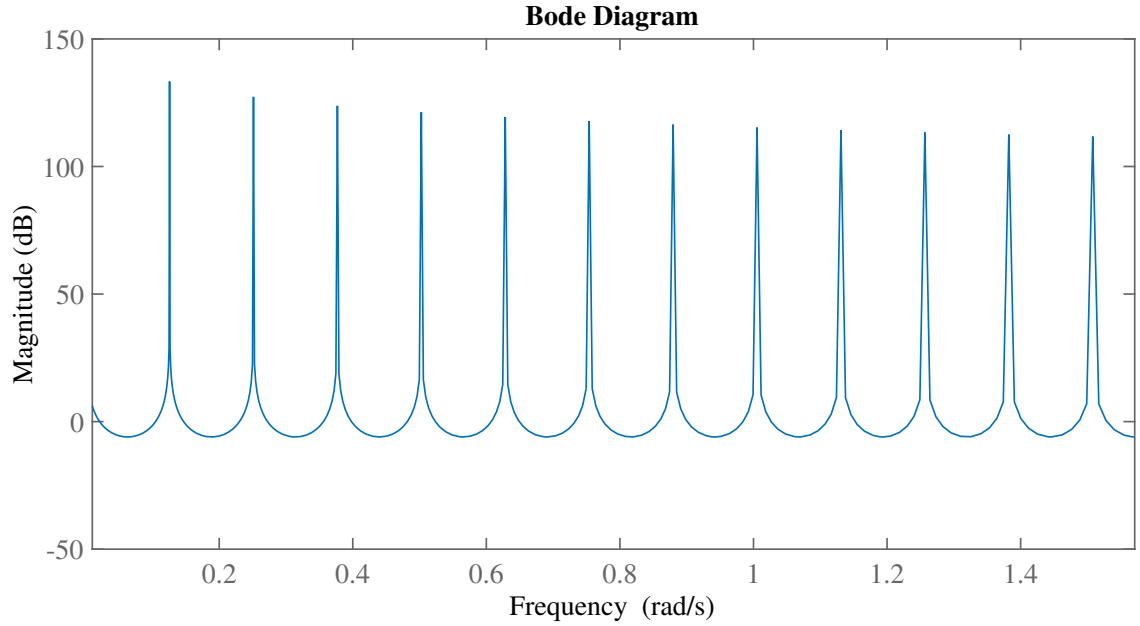


Figure 2.10: Bode Plot (linear scale) of the periodic signal generator for $N = 50$.

It is significant to allude that Bode Plots show only the steady-state gain of the system. Therefore, they should be carefully used if there are important requirements on the transient performance of the control system.

2.3.4 Null-Phase FIR Filter

The periodic signal generator introduces a large gain in $N - 1$ frequencies [8]. This, however, could not be wanted in the system because high-frequency noise might be undesirably amplified. Additionally, the plant model is usually not exactly known at the high portion of the spectrum. Hence, providing high gain without full knowledge of the behavior of the plant could endanger both the performance and the stability of the overall system. That being the case, a Low-Pass Filter (LPF) should be introduced in order to cut off the unwanted high-frequency resonant peaks of the periodic signal generator.

In continuous time, all LPFs bring in together a magnitude gain and a phase shift. The latter can also be problematic for the stability of the overall system since the phase shifts could be understood as delays on the output. In discrete time, though, there exists a topology known

as *null-phase Finite Impulse Response (FIR) filter* that produces no phase shift when passing the frequencies below its cutoff point. Its transfer function is given by:

$$H[z] = l_2 z^{-2} + l_1 z^{-1} + l_0 + l_1 z + l_2 z^2 = \frac{l_2 + l_1 z + l_0 z^2 + l_1 z^3 + l_2 z^4}{z^2} \quad (2.13)$$

In Figure 2.11, the Bode Plot for a null-phase FIR filter is presented. Notice that the phase shift for all frequencies is $360^\circ = 0^\circ$.

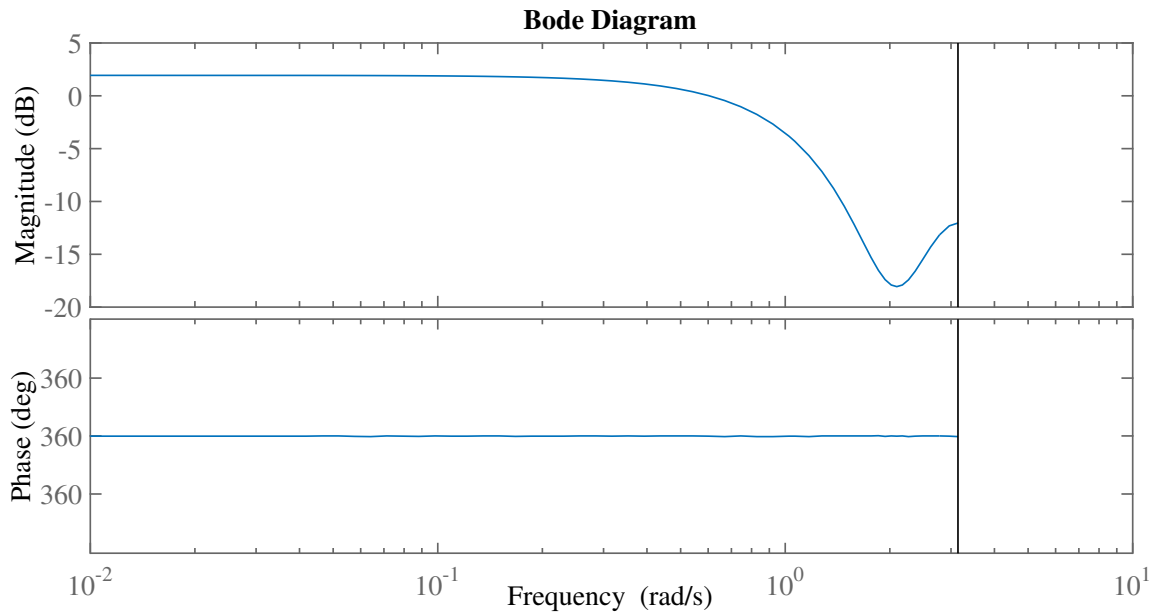


Figure 2.11: Bode Plot (logarithmic scale) of a null-phase FIR filter with transfer function $0.125z^{-2} + 0.25z^{-1} + 0.5 + 0.25z + 0.125z^2$.

The transfer function stated in Equation 2.13 is non-causal because the order of the numerator z -polynomial is greater than the order of the denominator z -polynomial. Non-causal systems are not desired in practice. This is overcome by multiplying the H -filter transfer function by z^{-N} .

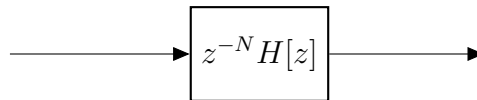


Figure 2.12: Causal null-phase FIR filter.

The design of this filter usually implies a tradeoff between performance and robustness.

2.3.5 Plug-in Internal Model

Both the action of the internal model (periodic signal generator) and the null-phase filter may be combined. Such a configuration is called *plug-in internal model* [2] [10].

If the output of system shown in Figure 2.12 is positively fed back (Figure 2.13), the overall transfer function becomes:

$$H_o[z] = \frac{z^{-N}H[z]}{1 - z^{-N}H[z]} \quad (2.14)$$

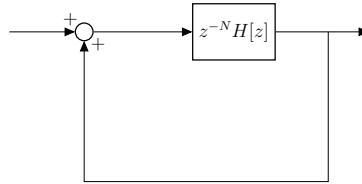


Figure 2.13: Plug-in internal model.

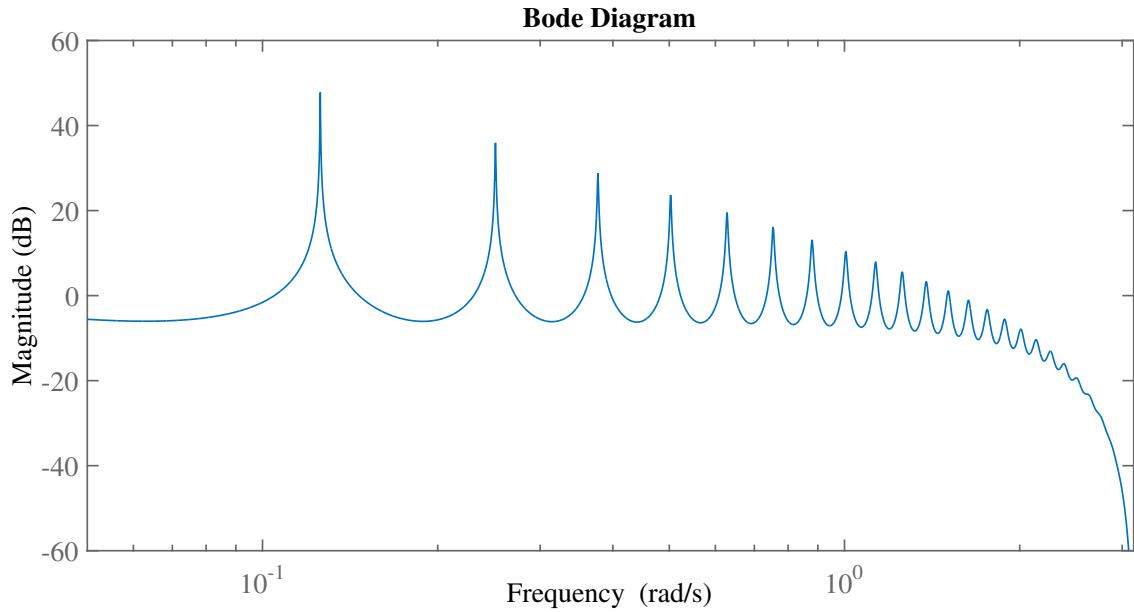


Figure 2.14: Magnitude Bode Plot (logarithmic scale) of the plug-in internal model.

Figure 2.14 and Figure 2.15 display the magnitude Bode Plot of this system using a H -filter with transfer function $0.25z^{-1} + 0.5 + 0.25z$. It should be pointed out that the action of the

internal model is preserved in some frequencies after which the attenuation of the LPF takes place.

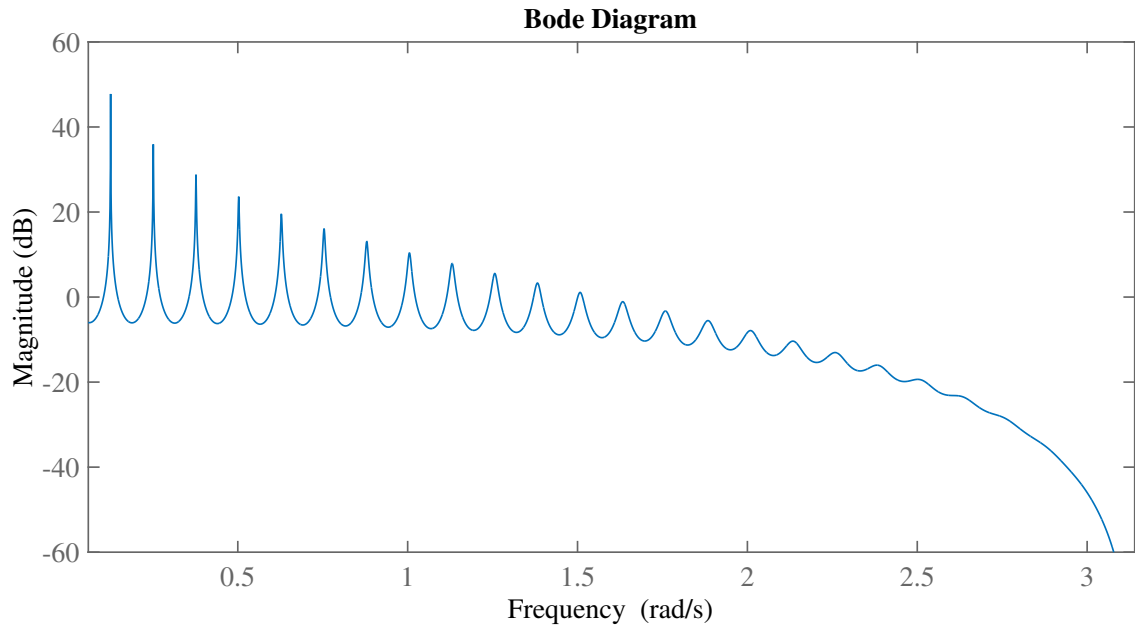


Figure 2.15: Magnitude Bode Plot (linear scale) of the plug-in internal model.

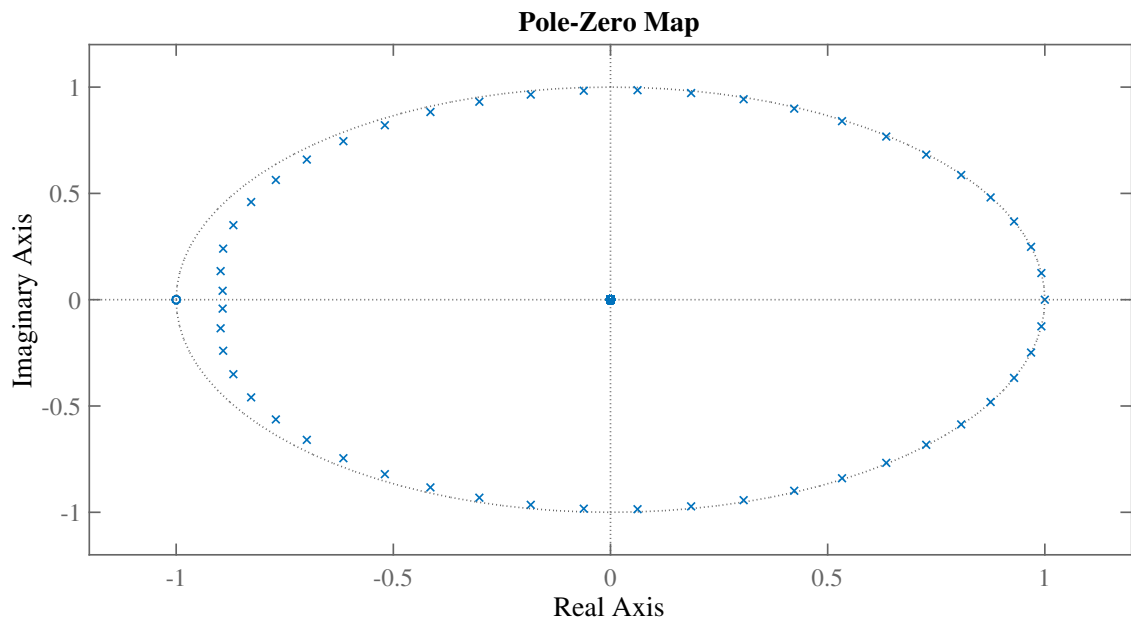


Figure 2.16: Pole-zero map of the plug-in internal model.

Figure 2.16 illustrates the fact that the N equally distributed poles on the unit circumference, which is the main characteristic of the periodic signal generator, is maintained. Nevertheless,

some poles are brought into the unit circle which confirms that the filter attenuates large gain at high frequencies.

2.3.6 Small-Gain Theorem

Up to this point two positive feedback systems have been introduced: the periodic signal generator and the plug-in internal model. To study the stability of such systems, a general positive feedback system is presented in Figure 2.17.

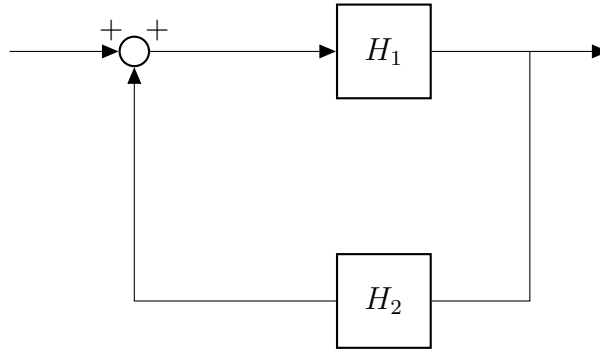


Figure 2.17: General positive feedback system.

The *small-gain theorem* states that the overall closed-loop positive system is stable if the *infinite norm* of H_1H_2 is less than 1:

$$||H_1H_2||_{\infty} < 1 \quad (2.15)$$

The *infinite norm* of a transfer function is defined as the maximum value of its magnitude Bode Plot.

2.3.7 Repetitive Control Architecture

In order to apply the IMP using the plug-in internal model, the system must be in unity negative feedback configuration. The RC architecture is presented in Figure 2.18. It is also known as *plugged control*.

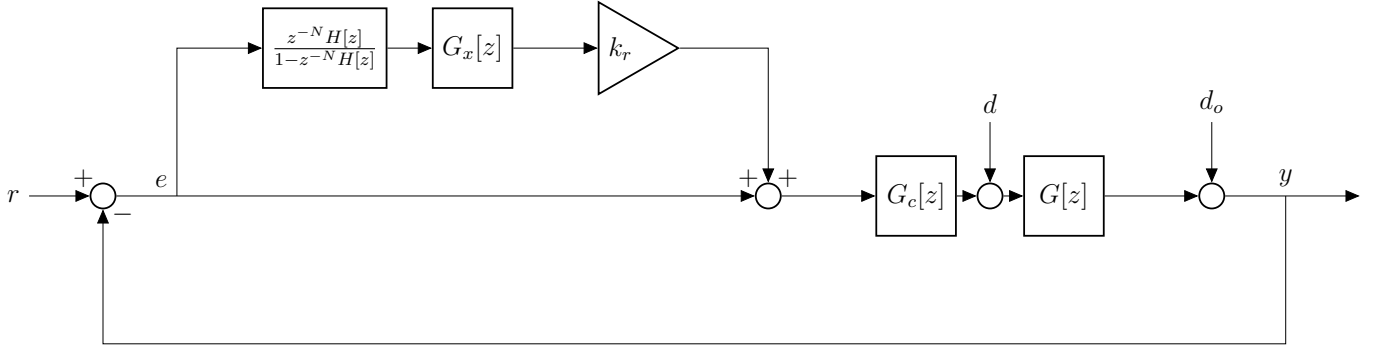


Figure 2.18: Repetitive Control architecture.

In this block diagram:

- r , e , d , d_o and y are the reference, error, plant disturbance, output disturbance and output signals with corresponding z-transforms $R[z]$, $E[z]$, $D[z]$, $D_o[z]$ and $Y[z]$.
- $G_x[z]$: is a controller added for stability.
- $G_c[z]$: is a controller designed for the closed-loop system *without* the RC.
- $G[z]$: is a discrete time transfer function of the plant.

The controller $G_c[z]$ is designed for the unity-feedback system without the RC internal model loop and it must:

- achieve the desired transient performance according to application requirements.
- have good stability margins to guarantee robustness.
- reduce the plant uncertainties at high frequencies.

2.3.8 Stability Analysis

The stability analysis of the system presented in Figure 2.18 is not straightforward. It has been shown [10] that the analysis may be performed by means of the *sensitivity function* $S[z]$ which is the transfer function from the reference to the error [26, p. 23]:

$$S[z] = G_{re}[z] = \frac{E[z]}{R[z]} = (1 - z^{-N}H[z]) \frac{1}{1 - z^{-N}H[z](1 - k_r G_x[z]G_o[z])} \frac{1}{1 + G_c[z]G[z]} \quad (2.16)$$

where $G_o[z]$ is the transfer function of the system without RC

$$G_o[z] = \frac{G_c[z]G[z]}{1 + G_c[z]G_o[z]}$$

Equation 2.16 may be broken up into three components S_1 , S_2 and S_3 where:

- S_2 : function dependent on the internal model, the stability part G_x and the closed-loop transfer function without RC G_o .
- S_3 : the sensitivity function of the closed-loop system without RC.

$$S[z] = G_{re}[z] = \underbrace{(1 - z^{-N}H[z])}_{S_1} \times \underbrace{\frac{1}{1 - z^{-N}H[z](1 - k_r G_x[z]G_o[z])}}_{S_2} \times \underbrace{\frac{1}{1 + G_c[z]G[z]}}_{S_3}$$

In order of the RC control system to be stable, all S_1 , S_2 and S_3 must be stable. S_2 stability will be analyzed in the last turn.

S_1 Stability

Replacing Equation 2.13 into the S_1 definition:

$$1 - z^{-N}H[z] = 1 - z^{-N}(l_2 z^{-2} + l_1 z^{-1} + l_0 + l_1 z + l_2 z^2) = 1 - l_2 z^{-N-2} + l_1 z^{-N-1} + l_0 z^{-N} + l_1 z^{-N+1} + l_2 z^{-N+2}$$

The previous expression can be regarded as a polynomial of z^{-N} which is always BIBO stable.

S_3 Stability

Recall that S_3 corresponds to the sensitivity function of the overall system without RC.

$$S_3 = \frac{1}{1 + G_c[z]G[z]}$$

The design of the controller G_c must provide stability for the closed-loop. For this reason, S_3 is stable.

S_2 Stability

Under given conditions, the stability analysis of S_2 is reduced to the consideration of the stability of [8] [14]:

$$\|z^{-N}H[z](1 - k_r G_x[z]G_o[z])\|_\infty < 1$$

Recall that the infinite norm of a transfer function is computed from its bode plot. By rearranging the previous expression it is obtained:

$$\|z^{-N}H[z]\|_\infty \times \|1 - k_r G_x[z]G_o[z]\|_\infty < 1$$

The infinite norm of the pure delay is equal to the unity $\|z^{-N}\|_\infty = 1$. The H -filter by design has also a unity infinite norm [8] [14]. Hence, the analysis is reduced to:

$$\|1 - k_r G_x[z]G_o[z]\|_\infty < 1$$

The smaller the value of the infinite norm, the more robust the system. Hence, the most straightforward form to guarantee that the previous inequation is satisfied is by defining G_x in the following form:

$$G_x = \frac{k_r}{G_o} \quad (2.17)$$

where k_r is a gain selected in trade off between robustness and performance and it is sometimes included within the controller definition.

Remark that G_x defined in this way is a noncausal transfer function. Nevertheless, the delays z^{-N} in the internal model undertake this issue. As a consequence, N should be adequately large to make causal both $H[z]$ and G_x . From experimental results, it has been found that $N = 20$ is an appropriate lower limit for the number of samples per period in order to implement a repetitive controller.

2.4 Angular Space Repetitive Control

2.4.1 Relation between Angular Space and Time Domain

A sinusoidal time-dependent signal $u(t) = U \sin(\omega t + \phi)$ is considered. The case where $\phi = 0$ is shown in Figure 2.19.

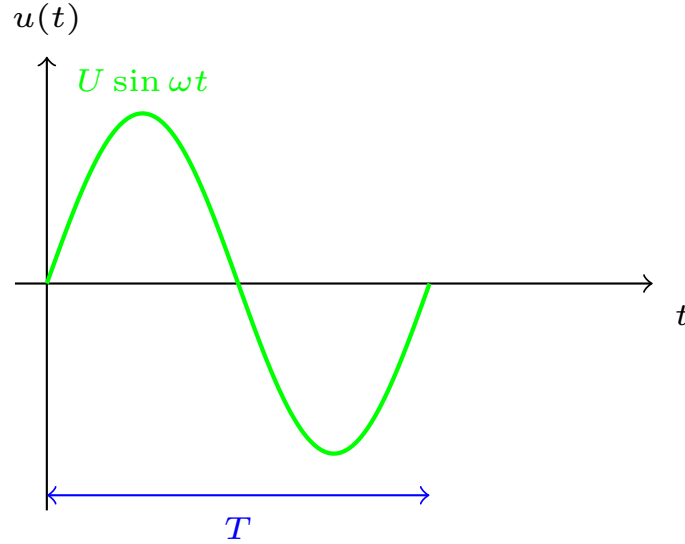


Figure 2.19: Sinusoidal waveform in time domain.

where $\omega = 2\pi f$ is the angular frequency and $T = 2\pi/\omega$ is the fundamental period.

The argument of the sin function, named θ , is understood here as the *angle* at which the trigonometric function is being computed. θ is related with its time dependent derivative ω as follows:

$$\frac{d\theta}{dt} = \omega(t) \quad (2.18)$$

From the last formula, the relation between the angular space domain and the time domain can be found [14]:

$$\theta(t) = \int_0^t \omega(\tau) d\tau + \theta(0) \quad (2.19)$$

A mathematical expression for ω as a function of time is difficult to obtain. Two alternatives for overcoming this disadvantage are:

- To consider the frequency as a piecewise constant function.
- To compute online an instantaneous value of ω .

The latter approach is going to be applied in this document.

2.4.2 Mapping into Angular Space Domain

The mapping of a sinusoidal-time function into angular space domain might be seen as a three-step process. First, an angle corresponding to any given instant of time is calculated. Afterwards, the sine of this angle gives the value of the function in angular space domain.

$$t \rightarrow \theta(t) \rightarrow u(\theta) \quad (2.20)$$

The sine function is periodic whether it is computed time or in angular space domain. In time-domain, its fundamental period depends on the frequency of the signal $T = 1/f$. The computation of the argument of the sine function in time domain yields an angle in angular space domain, in which the period is always the same $T = 2\pi$ because this angle might be related to a reference angle in the range $0 - 2\pi$.

To understand the mapping concept of the angular space transform, three sinusoids of different frequencies ω_1 , ω_2 and ω_3 are plotted in Figure 2.19.

Consider the maximum of the sine function. The time of occurrence is different on each waveform (t_{m1} , t_{m2} and t_{m3}) and depends on the frequency of the signal. However, for all signals in the angular domain, the maximum occurs at an angle of $\theta_m = 90^\circ = \pi/2$.

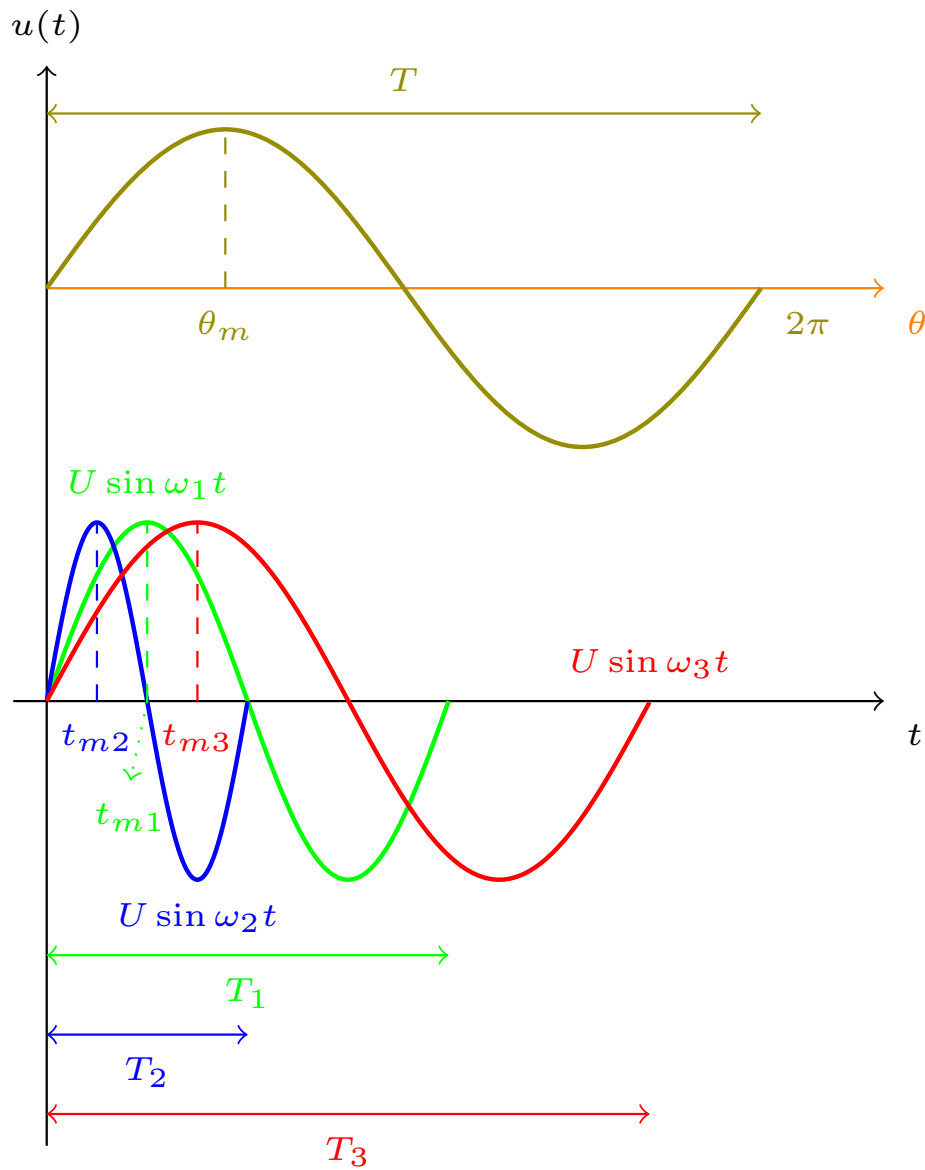


Figure 2.20: Mapping from the time to the angular domain.

This means that all time points whose argument evaluation yields an angle of $90^\circ = \pi/2$ are mapped into the same point in angular space domain $\theta = 90^\circ = \pi/2$ (Figure 2.21). The same consideration applies for all other instants of time.

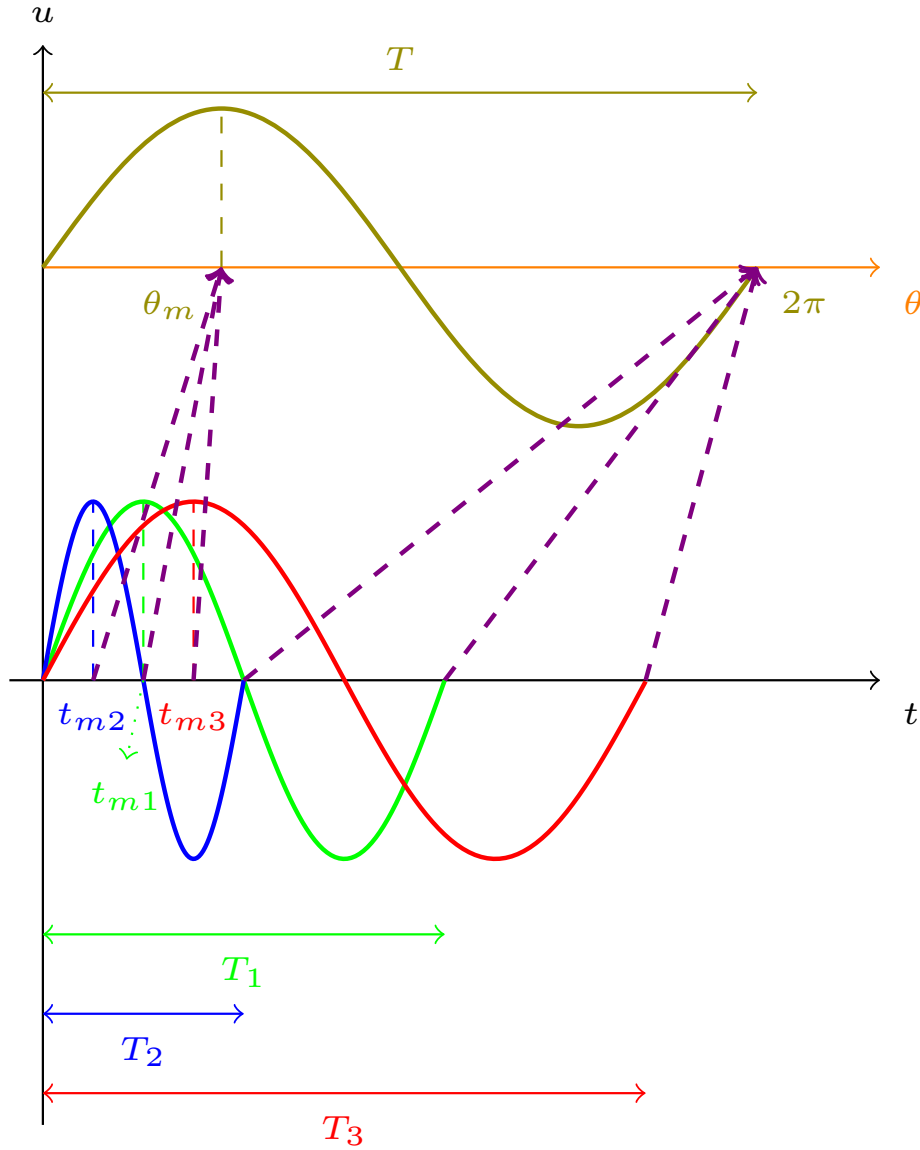


Figure 2.21: Frequency in the mapping from time to angular space domain.

In this way, all sinusoids of equal amplitude and different frequencies are mapped into a single sinusoid with period $T = 2\pi$ in angular space domain. This transformation might also be thought as an axis scaling: for large frequencies, the time axis stretches whereas for small frequencies, the time axis elongates.

2.4.3 Angular Space Transform

In the mapping process, a change of variable has been made to make u a function of θ :

$$t \rightarrow \theta(t) \rightarrow \sin \theta$$

In this way, a sinusoidal signal expression in angular space domain is:

$$u(\theta) = U \sin \theta \quad (2.21)$$

The period, frequency and angular frequency have been shown to be constant:

$$T = 2\pi \quad (2.22)$$

$$f = \frac{1}{2\pi} \quad (2.23)$$

$$\omega = 1 \quad (2.24)$$

Using the chain rule, the derivative of u respect to time is given by:

$$\frac{du}{dt} = \frac{du}{d\theta} \cdot \frac{d\theta}{dt} \quad (2.25)$$

Equation 2.25 has introduced a definition for the transformation of a derivative from the time-domain into the space angular domain:

$$\frac{d}{dt} = \omega(t) \frac{d}{d\theta} \quad (2.26)$$

where

$$\omega(t) = \frac{d\theta}{dt} \quad (2.27)$$

One should become aware of the issue that the following condition must be accomplished in order to assure the existence of the inverse mapping function $[t = f^{-1}(\theta)]$ from the angular space to the time domain [14]:

$$\omega(t) = \frac{d\theta}{dt} > 0 \quad (2.28)$$

It is worth to emphasize that this condition will always be met on practical electric systems, even when the frequency could change: the electrical frequency f_e will always be positive.

2.4.4 Space-State System Representation in Angular Space

Consider the state equation of a linear-time invariant system with a vector of state variables \mathbf{x} in time domain:

$$\frac{d\mathbf{x}}{dt} = \mathbf{A}\mathbf{x} + \mathbf{B}\mathbf{u} \quad (2.29)$$

Replacing the derivative transform from Equation 2.26, with the angular space state vectors represented as $\bar{\mathbf{x}}$ and $\bar{\mathbf{u}}$:

$$\omega(t) \frac{d}{d\theta} \bar{\mathbf{x}}(\theta) = \mathbf{A} \bar{\mathbf{x}}(\theta) + \mathbf{B} \bar{\mathbf{u}}(\theta) \quad (2.30)$$

The new state equation in angular space domain is:

$$\frac{d\bar{\mathbf{x}}}{d\theta} = \mathbf{A}_\theta \bar{\mathbf{x}}(\theta) + \mathbf{B}_\theta \bar{\mathbf{u}}(\theta) \quad (2.31)$$

where the matrices \mathbf{A}_θ and \mathbf{B}_θ can be related to the matrices \mathbf{A} and \mathbf{B} in time-domain:

$$\mathbf{A}_\theta = \frac{1}{\omega(t)} \mathbf{A} \quad (2.32)$$

$$\mathbf{B}_\theta = \frac{1}{\omega(t)} \mathbf{B} \quad (2.33)$$

The matrix \mathbf{A} of the system in time-domain may be written in Jordan canonical form \mathbf{J} via a equivalent transformation:

$$\mathbf{J} = \mathbf{PAP}^{-1} \quad (2.34)$$

The main characteristic of the Jordan canonical form \mathbf{J} is that the eigenvalues of the matrix \mathbf{A} (i.e. the poles of the closed-loop system) $\lambda_1, \lambda_2, \dots, \lambda_n$ are located in the main diagonal.

$$\mathbf{J} = \begin{bmatrix} \lambda_1 & 0 & \dots & \dots & \dots & 0 \\ 0 & \lambda_2 & 0 & \dots & \dots & \vdots \\ \vdots & \vdots & \ddots & \dots & \vdots & \vdots \\ 0 & 0 & \dots & \lambda_i & 0 & 0 \\ \vdots & \vdots & \dots & \dots & \ddots & \vdots \\ 0 & 0 & \dots & \dots & 0 & \lambda_n \end{bmatrix} \quad (2.35)$$

Bringing the matrix in the Jordan canonical form \mathbf{J} to the angular space yields:

$$\frac{1}{\omega(t)} \mathbf{J} = \frac{1}{\omega(t)} \begin{bmatrix} \lambda_1 & 0 & \dots & \dots & \dots & 0 \\ 0 & \lambda_2 & 0 & \dots & \dots & \vdots \\ \vdots & \vdots & \ddots & \dots & \vdots & \vdots \\ 0 & 0 & \dots & \lambda_i & 0 & 0 \\ \vdots & \vdots & \dots & \dots & \ddots & \vdots \\ 0 & 0 & \dots & \dots & 0 & \lambda_n \end{bmatrix} \quad (2.36)$$

The eigenvalues of the system in the new space are:

$$\lambda_{i,\theta}^- = \frac{\lambda_i}{\omega(t)} \quad (2.37)$$

On this account, when $\omega(t)$ changes, the poles of the system are displaced when the angular space transformation is applied:

- $\omega(t) \uparrow$: the poles approximate the origin and the system response becomes slower.
- $\omega(t) \downarrow$: the poles separate from the origin and the system response becomes faster.
- If the frequency is held constant, the poles of the system in angular space are fixed and linearly related to those in time domain.

A concluding fact from the angular space transformation is that, whereas the frequency of all sinusoids can be regarded as constant, the poles and the zeros of the plant are moving in the complex plane of the angular space. Hence, the resulting system representation is known as a Linear Parameter Varying (LPV) representation which can also be concluded from Equations 2.32 and 2.33 which explicitly state the time-varying parameter $\omega(t)$.

2.4.5 Laplace Operator in Angular Space Domain

The Laplace transform may also be defined in angular space domain [13]:

$$G(\bar{s}) = \int_0^\infty g(\theta) e^{-\bar{s}\theta} d\theta \quad (2.38)$$

where \bar{s} will be used for denoting the complex variable in angular domain to distinguish it from the s variable in time-domain.

Equation 2.38 has the same form as the Laplace transform for time-domain functions. Hence, all the properties of this integral operator are applicable in angular space domain.

2.4.6 Z-Transform in Angular Space Domain

RC is a discrete control technique. That being so, an adequate definition of the z-transform in angular space is introduced:

$$G[\bar{z}] = \sum_0^{\infty} g[\theta] \bar{z}^{-\theta} \quad (2.39)$$

Again, \bar{z} is used to distinguish the complex variable in angular space from its time-domain counterpart.

2.4.7 Angular Space Repetitive Control

RC introduces infinite gains at the fundamental and a large number of harmonics of a reference signal. However, when the frequency of the signal changes, so do the frequencies of its harmonics. Hence, the RC architecture is said to have performance drawbacks when the frequency of the system changes [9].

Angular transformation enables to regard the frequency of any sinusoid as constant. That being so, the architecture of Repetitive Control might be applied in angular space to track sinusoids of a large number of frequencies simultaneously rejecting harmonic perturbances.

In angular domain, the period of any sinusoidal signals might be regarded as constant. Hence, the number of samples per period will be:

$$N = \frac{T_p}{T_s} = \frac{2\pi}{T_s} \quad (2.40)$$

This relationship shows that the number of samples of the repetitive control in angular space should be held constant by taking an equal number of samples per period, independent of the frequency of the time-sinusoidal. To achieve this purpose, a pPLL-based testing platform that will be presented in Chapter 3 has been designed.

This kind of platform allows the repetitive controller to operate in constant angular frequency conditions, a time variation of the frequency moves the plant poles in angular space. To overcome this issue, a technique known as *plant precompensation* is presented. The corresponding block diagram is shown in Figure 2.22.

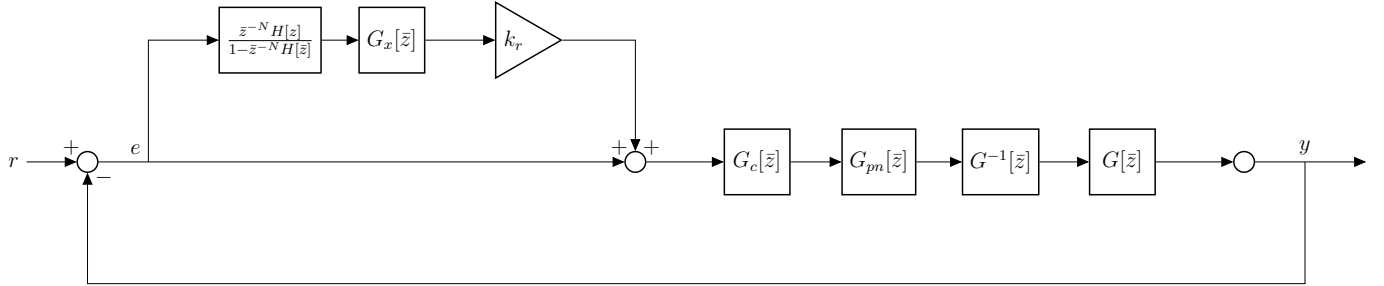


Figure 2.22: Angular Space Repetitive Control architecture with plant precompensation.

In this block diagram:

- $G_{pn}[\bar{z}]$ is the nominal plant: the model of the plant under nominal frequency conditions in angular domain.
- $G^{-1}[\bar{z}]$ is the inverse of the plant in space domain.
- $G[\bar{z}]$ plant in angular space domain.

Plant precompensation involves pole-zero cancellation. This can only be allowed when the poles and zeros to be cancelled are both stable. This technique will be analyzed in detail in Chapter 3.

Chapter 3

Design

3.1 Introduction

The main purpose of this Chapter is to design an Angular Space Repetitive Control (ASRC) for an Active Power Filter (APF), operating in a single-phase system subjected to a nonlinear load (filtered full-wave rectifier) in order to make it robust against grid frequency deviations. The main control objective is to make the source current i_s as sinusoidal as possible. The proposed circuit topology is shown in Figure 3.1.

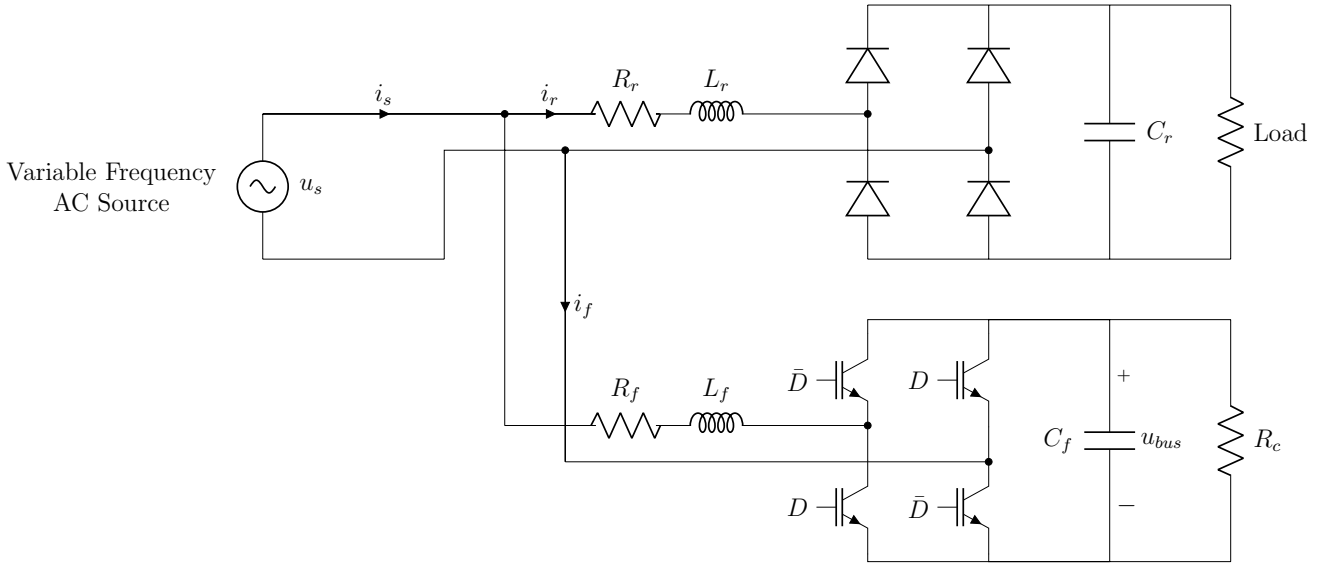


Figure 3.1: Full system

In Figure 3.1:

- u_s : variable frequency source voltage.
- i_s : source current.
- i_r : rectifier current.
- i_f : APF current.
- u_{bus} : APF DC bus voltage.
- D, \bar{D} : gate control signals of the IGBT transistors.
- R_f, L_f : resistance and inductance of the Active Power Filter (APF).
- R_r, L_r : resistance and inductance of the rectifier (for filtering high-frequency components).
- C_r : load filtering capacitance.
- C_f : APF capacitance.
- R_c : filter discharging resistance.

In this chapter, a modelling process of the APF will be resumed alongside with an introduction to the plant precompensation scheme. Afterwards, the design of the required pPLL-based testing platform for angular space control techniques will be detailed. With this platform fulfilling the requirements of RC to operate in angular space domain, a controller for the current loop and the voltage loop will be designed.

The component values used for the modelling and simulation process were $R_f = 1.4 \Omega$, $L_f = 1.2 \text{ mH}$, $C_f = 1000 \mu\text{F}$, $R_c = 8.2k\Omega$, $R_r = 1.4 \Omega$ and $L_r = 1.2 \text{ mH}$ and $C_r = 470 \mu\text{F}$.

3.2 Plant Modelling

A shunt-connected APF intends to correct the power factor of a load so that the feeding source sees a unity power factor from the loading side. Also, it is expected for the APF to reduce the harmonic content of a nonlinear load. Accordingly, it is expected that this system includes reactive components in order to be able to exchange dynamically reactive power with the grid. For that reason, a capacitor and an inductor are included in the topology shown in Figure 3.2. Such topology is known also as single-level because there exists only one DC voltage level at the capacitor bus.

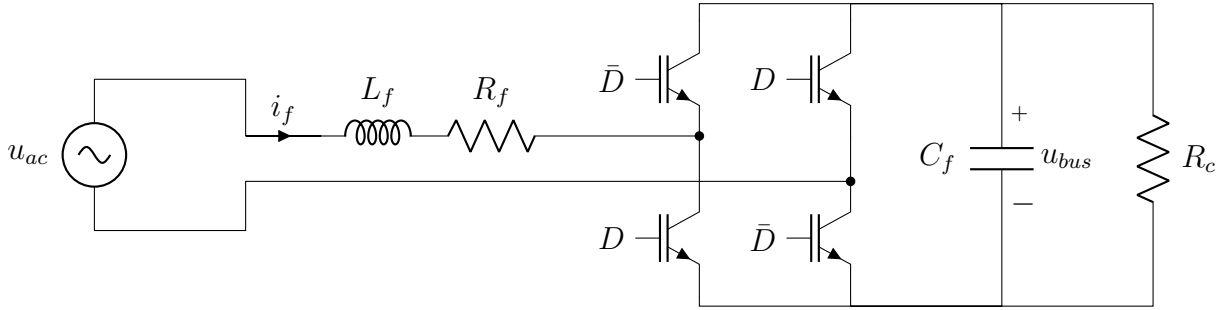


Figure 3.2: Single-phase shunt-connected Active Power Filter (APF).

Current Loop

In the upcoming sections, the averaged models for the current and the voltage loops at the commutation frequency are developed.

Kirchhoff's Voltage Law relates the variables in the system through upcoming equation:

$$u_{ac} = R_f \cdot i + L_f \frac{di}{dt} + f(D)u_{bus}$$

where $f(D)$ is a logic function dependent on the switching state of the IGBTs. The control variable D can take the logic values 1 (on) and 0 (off):

$$f(D) = \begin{cases} -1 & D = 1 \\ 1 & D = 0 \end{cases}$$

A logic expression that describes both states in a single equation is:

$$f(D) = 1 - 2D$$

Replacing in Kirchhoff's Voltage Law expression:

$$u_{ac} = R_f \cdot i + L_f \frac{di}{dt} + (1 - 2D)u_{bus}$$

Now, a time-dependent variable $\alpha(t)$ is defined:

$$\alpha(t) = (1 - 2D)u_{bus} - u_{ac} \quad (3.1)$$

Replacing this definition in the KVL expression yields:

$$-\alpha(t) = R_f \cdot i + L_f \frac{di}{dt} \quad (3.2)$$

Time-Domain Laplace time-domain transform can be applied to Equation 3.2 to obtain a continuous time transfer function of the current loop. Let the initial current through the inductor be zero. Then:

$$\begin{aligned} \mathcal{L}[-\alpha(t)] &= \mathcal{L}\left[R_f \cdot i + L_f \frac{di}{dt}\right] \\ -\alpha(s) &= R_f I(s) + sL_f I(s) = I(s)(R_f + sL_f) \end{aligned}$$

The time-domain transfer function of the current loop is consequently:

$$\frac{I(s)}{\alpha(s)} = G_i(s) = \frac{-1}{sL_f + R_f} \quad (3.3)$$

The transfer function in Equation 3.3 is of first order. Hence, it can be parametrized in terms of the time constant τ :

$$G_i(s) = \frac{K_{ti}}{\tau_{ti}s + 1} \quad (3.4)$$

where:

$$\tau_{ti} = \frac{L}{R} \quad (3.5)$$

$$K_{ti} = \frac{-1}{R} \quad (3.6)$$

The subscript t in both parameters stands for time to no confuse them with the parameters that will arise in the angular space modelling.

Angular Space Domain The angular space transform defined in Equation 2.26 ($\frac{d}{dt} = \omega \frac{d}{d\theta}$) is in this moment applied to Equation 3.2:

$$-\alpha(\theta) = R_f i(\theta) + L_f \omega \frac{di(\theta)}{d\theta} \quad (3.7)$$

The Laplace transform is now calculated on angular space domain:

$$-\alpha(\bar{s}) = R_f I(\bar{s}) + L_f \omega \bar{s} I(\bar{s})$$

The transfer function in continuous angular space domain is:

$$G_i(\bar{s}) = \frac{I(\bar{s})}{\alpha(\bar{s})} = \frac{-1}{R_f + L_f \omega \bar{s}} \quad (3.8)$$

The pole of the transfer function in Equation 3.8 moves in the complex plane as ω changes, as predicted in Chapter 2. Also, as it is a first-order transfer function, it may be parametrized in terms of the angular domain time-constant τ_i and a gain K_i :

$$G_i(\bar{s}) = \frac{K_i}{\tau_i \bar{s} + 1} \quad (3.9)$$

where

$$K_i = \frac{-1}{R_f} = K_{ti} \quad (3.10)$$

$$\tau_i = \frac{\omega L_f}{R_f} = \omega \tau_{ti} \quad (3.11)$$

As $\omega(t)$ changes, parameter τ_i varies.

Angular Discretization of Transfer Function The transfer function in Equations 3.8 and 3.9 is continuous. RC requires a discrete version of the plant for the design of controllers. Since the current loop transfer function is first-order, the discrete angular transfer function takes the following form:

$$G_i[\bar{z}] = \frac{K_i(1 - e^{-T/\tau_i})}{\bar{z} - e^{-T/\tau_i}} \quad (3.12)$$

where

$$T = T_s = \frac{2\pi}{N} \quad (3.13)$$

is the sample time. N is the number of samples per period of the fundamental signal. As mentioned before, if the number of samples per period is constant, so it is the sampling period as the fundamental period of the signal in angular domain is always 2π . Angular Space Repetitive Control requires a platform that takes always the same number of samples per period of the reference grid voltage sinewave, independent of its frequency. The design of such platform will be covered later in this Chapter.

3.2.1 Voltage Loop

Figure 3.2 is replied in order to obtain an averaged model at the conmutating frequency for controlling the voltage on the DC bus of the APF.

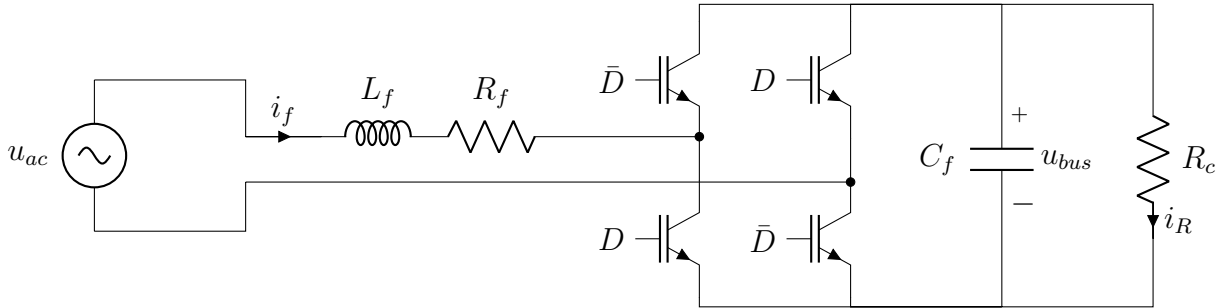


Figure 3.3: Modelling of the voltage loop.

Kirchhoff's Current Law applied on the capacitor node (positive pole of the DC bus) yields:

$$i_c(t) + i_R(t) = f(D)i_f(t)$$

where $f(D)$ is a logic function depending on the switching state of the IGBTs.

$$f(D) \begin{cases} -1 & D = 1 \\ 1 & D = 0 \end{cases}$$

An equivalent logic expression will be:

$$f(D) = 1 - 2D$$

Replacing in the KCL equation:

$$i_c(t) + i_R(t) = C_f \frac{du_{bus}(t)}{dt} + \frac{1}{R_c} u_{bus}(t) = (1 - 2D)i_f(t)$$

Defining the β variable as:

$$\beta(t) = (1 - 2D)i_f(t) \tag{3.14}$$

results in the following time-domain equation for the voltage loop:

$$C_f \frac{du_{bus}(t)}{dt} + \frac{1}{R_c} u_{bus}(t) = \beta(t) \tag{3.15}$$

Time-Domain Via Laplace time-domain transform the following transfer function is obtained for the voltage loop:

$$\begin{aligned}
C_f s U_{bus}(s) + \frac{1}{R_c} U_{bus}(s) &= \beta(s) \\
U_{bus}(s) \left(C_f s + \frac{1}{R_c} \right) &= \beta(s) \\
G_u(s) = \frac{U_{bus}(s)}{\beta(s)} &= \frac{1}{C_f s + \frac{1}{R_c}} \\
\frac{U_{bus}(s)}{\beta(s)} = G_u(s) &= \frac{R_c}{R_c C_f s + 1}
\end{aligned} \tag{3.16}$$

This first-order transfer function can be parametrized as:

$$G_u(s) = \frac{K_{tu}}{\tau_{tu}s + 1} \tag{3.17}$$

where

$$\tau_{tu} = R_c C_f \quad K_{tu} = R_c \tag{3.18}$$

Angular Space Domain Equation 3.15 may be transformed into angular space domain by means of the transformation presented in Equation 2.26.

$$C_f \omega \frac{u_{bus}(\theta)}{d\theta} + \frac{1}{R_c} u_{bus}(\theta) = \beta(\theta)$$

Applying the angular Laplace operator

$$C_f \omega \bar{s} U_{bus}(\bar{s}) + \frac{1}{R_c} U_{bus}(\bar{s}) = \beta(\bar{s})$$

allows to find the transfer function for the voltage loop

$$G_u(\bar{s}) = \frac{U_{bus}(\bar{s})}{\beta(\bar{s})} = \frac{R_c}{R_c \omega C_f \bar{s} + 1} = \frac{K_u}{\tau_u \bar{s} + 1} \quad (3.19)$$

where

$$K_u = R_c = K_{tu} \quad \tau_u = \omega R_c C_f = \omega \tau_{tu} \quad (3.20)$$

The discretization for the voltage loop transfer function may be performed in the same fashion as the current transfer function. Therefore, the procedure will not be repeated.

3.2.2 Plant Precompensation

Plant precompensation will be used for the control loop in which the Angular Space Repetitive Control is to be applied. Figure 2.22 presented the plant precompensation scheme in which a stable pole-zero cancellation was involved. The overall scheme is shown again in Figure 3.4.

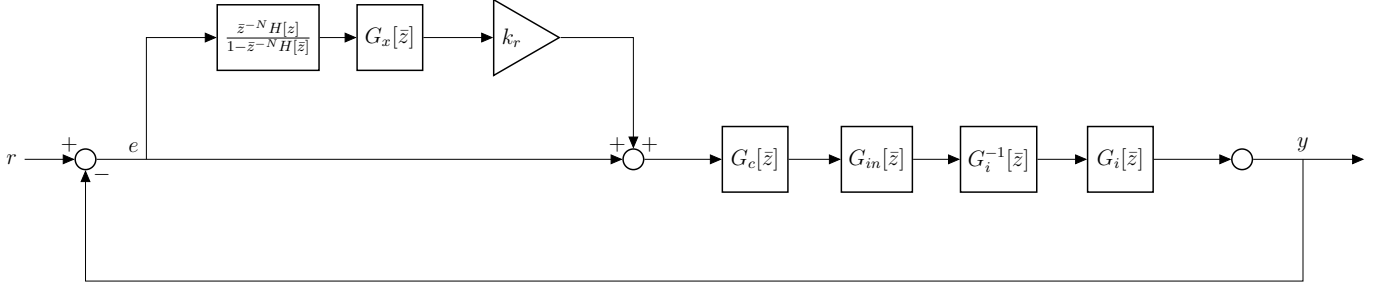


Figure 3.4: Angular Space Repetitive Control architecture with plant precompensation for the current loop.

In Figure 3.4:

- $G_{in}[\bar{z}]$: angular transfer function of the plant at the nominal frequency ω_n .
- $G_i^{-1}[\bar{z}]$: inverse angular transfer function of the plant.
- $G_i[\bar{z}]$: angular transfer function of the plant.

As the frequency changes, the plant poles are moving in the angle domain complex \bar{s} plane and the transfer function changes with time. Linear control design methods are not suitable for such transfer functions.

Plant precompensation takes advantage of the fact that, in this case, the plant is of first-order in both time and angular space domains with no zeros. Hence, the inverse function of the plant will have one stable zero. The cancellation between the pole of G_i^{-1} and G_i is allowed since both are stable, due to the fact that G_i in open-loop is stable. Also, both transfer functions are stable. Hence, the system is said to have *internal stability*, which reinforces the concept of pole-zero cancellation.

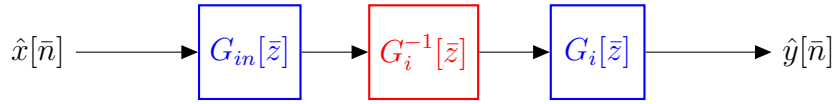


Figure 3.5: Plant precompensation scheme.

From Figure 3.5 can be inferred that the inverse plant, highlighted in red, is noncausal. However, the blue blocks representing the nominal angular plant and the plant are proper. The plant precompensation transfer function is:

$$\underbrace{\underbrace{\frac{K(1 - e^{-T/\tau_n})}{\bar{z} - e^{-T/\tau_n}}}_{\text{Causal}} \underbrace{\frac{\bar{z} - e^{-T/\tau}}{K(1 - e^{-T/\tau})}}_{\text{Noncausal}} \underbrace{\frac{K(1 - e^{-T/\tau})}{\bar{z} - e^{-T/\tau}}}_{\text{Causal}}}_{\text{Causal}} \quad (3.21)$$

It can be concluded that both the nominal plant and the inverse plant have to be implemented as one single transfer function on the main control loop because the inverse plant on its own is noncausal. Nevertheless, the inverse plant has a moving zero which directly depends on the actual frequency $\omega(t)$. Thus, it must be computed online using acquired information about the grid frequency: that is, the pPLL output.

The transfer function of the causal block composed of the nominal plant and the plant inverse in angular domain, after cancellation of the common K factor, is:

$$\frac{(1 - e^{-T/\tau_n})(\bar{z} - e^{-T/\tau})}{(\bar{z} - e^{-T/\tau_n})(1 - e^{-T/\tau})} \quad (3.22)$$

Equation 3.22 may be parametrized in the following manner:

$$B_n = e^{-T/\tau_n} \quad (3.23)$$

$$B = e^{-T/\tau} \quad (3.24)$$

$$A_n = 1 - e^{-T/\tau_n} = 1 - B_n \quad (3.25)$$

$$A = 1 - e^{-T/\tau} = 1 - B \quad (3.26)$$

Although $T = 2\pi/T_s$ is constant, parameters A and B must be computed online because the angular frequency of the grid is implicit in their expressions ($\tau = \frac{\omega(t)L_f}{R_f}$).

The resulting transfer function is:

$$G_{in}[\bar{z}]G_i^{-1}[\bar{z}] = \frac{A_n(\bar{z} - B)}{A(\bar{z} - B_n)} \quad (3.27)$$

To allow online computation of τ , and hence of A and B , a block diagram representation of the plant precompensation transfer function is going to be developed. The system in Figure 3.5 is said to have an input $\hat{x}[\bar{n}]$ and an output $\hat{y}[\bar{n}]$, both in angular spatial domain. They are related through the transfer function:

$$\frac{\hat{Y}[\bar{z}]}{\hat{X}[\bar{z}]} = \frac{A_n(\bar{z} - B)}{A(\bar{z} - B_n)}$$

Rewriting in terms of \bar{z}^{-1} :

$$\begin{aligned} \frac{\hat{Y}[\bar{z}]}{\hat{X}[\bar{z}]} &= \frac{A_n(\bar{z} - B)}{A(\bar{z} - B_n)} \times \frac{\bar{z}^{-1}}{\bar{z}^{-1}} \\ \frac{\hat{Y}[\bar{z}]}{\hat{X}[\bar{z}]} &= \frac{A_n - A_n B \bar{z}^{-1}}{A - A B_n \bar{z}^{-1}} \end{aligned} \quad (3.28)$$

Rearranging 3.28:

$$\begin{aligned}\hat{Y}[\bar{z}](A - AB_n\bar{z}^{-1}) &= \hat{X}[\bar{z}](A_n - A_nB\bar{z}^{-1}) \\ A\hat{Y}[\bar{z}] - AB_n\hat{Y}[\bar{z}]\bar{z}^{-1} &= A_n\hat{X}[\bar{z}] - A_nB\hat{X}[\bar{z}]\bar{z}^{-1}\end{aligned}$$

Expanding and taking inverse z-transform in angular domain:

$$\hat{y}[\bar{n}] = B_n\hat{y}[\bar{n} - 1] + \frac{A_n}{A}(\hat{x}[\bar{n}] - B\hat{x}[\bar{n} - 1]) \quad (3.29)$$

A block diagram realization of Equation 3.29 is drawn in Figure 3.6.

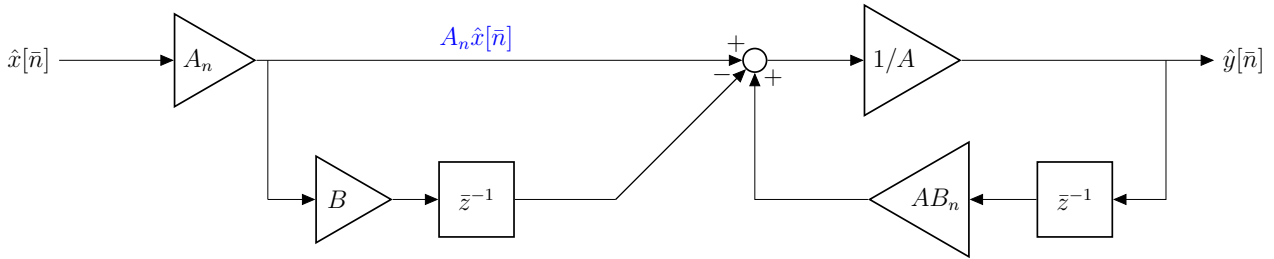


Figure 3.6: Block diagram of the plant implementation scheme.

3.3 Design of the pPLL-based Testing Platform

A pPLL was used to construct the testing platform for Angular Space Repetitive Control control in order to guarantee an equal number of signal samples, in spite of the period of the fundamental component of the grid voltage. The optimal tuning values used in this implementation can be consulted in [24].

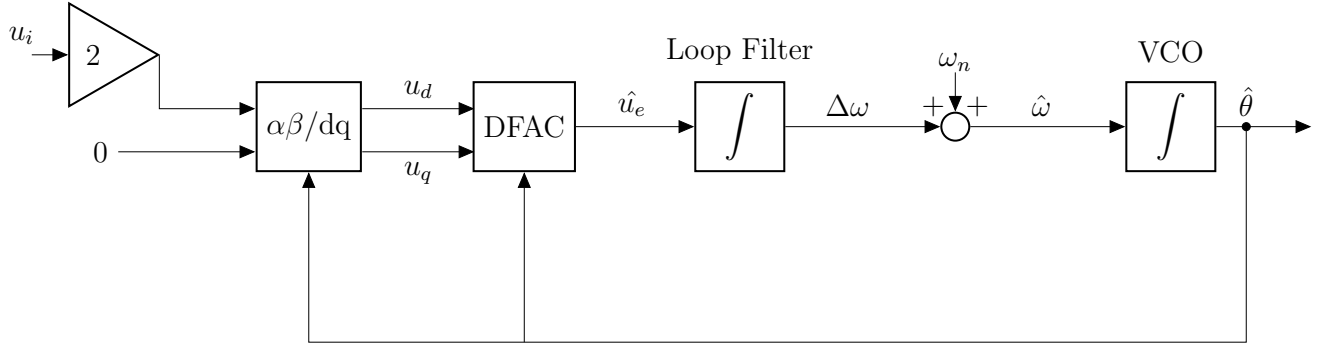


Figure 3.7: Implemented DFAC pPLL.

In Figure 3.7:

- u_i : input voltage signal.
- $u_{d,q}$: dq-transformation of the input voltage signal and a fictitious null imaginary signal.
- \hat{u}_e : estimated non-filtered voltage signal.
- $\Delta\omega$: estimated frequency deviation.
- ω_n : nominal angular frequency.
- $\hat{\omega}$: estimated angular frequency.
- $\hat{\theta}$: estimated angle.

The main idea behind this system is to sample the output of the pPLL $\hat{\theta}$ at a fixed number of grades in order to generate a clock pulse that interrupts the control system. When the interrupt arrives, the information of the measurements is made available so that the control outputs can be computed.

The number of interruptions per period is always the same. This implies that if the frequency changes, so does correspondingly the width of the pulses. Two different methods for the implementation of this system are going to be described:

- *Software clock*: a variable-width clock is computed via logic functions from the output of a pPLL-based system.
- *Hardware interruptions*: the duty-cycle parameter of a PWM hardware module within a Digital Signal Processor (DSP) is dynamically adjusted. The rising edges of the PWM output force interruptions of the internal CPU. Hence, the control system takes information from variable measurements and performs control actions when commanded by the PWM module.

Both design procedures use the output of the pPLL shown in Figure 3.8.

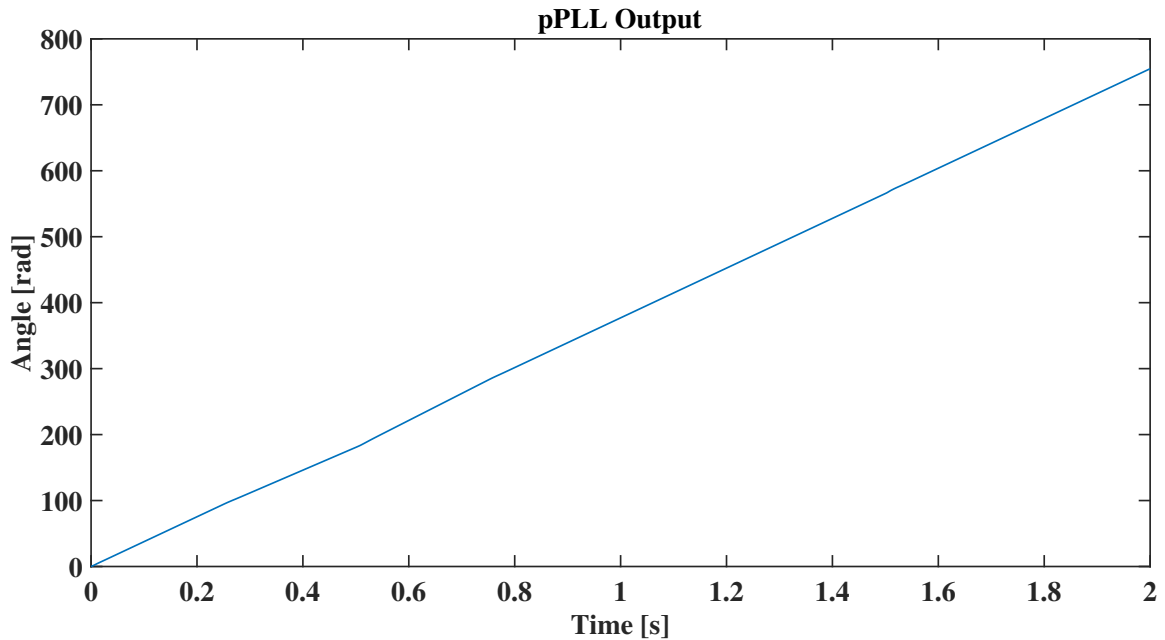


Figure 3.8: pPLL output

The frequency of the signal represents the slope of Figure 3.8: the higher the frequency, the more bent the pPLL output.

3.3.1 Software Clock

The pPLL output is first converted from radians to degrees to reduce computation load since divisions will be performed. Afterwards, a modulus operation is made. This operation returns

the remainder of a division between the dividend (pPLL output) and the divisor (angle that gives a number of N samples in 360°). When the division is exact, the result is zero (green points in Figure 3.9).

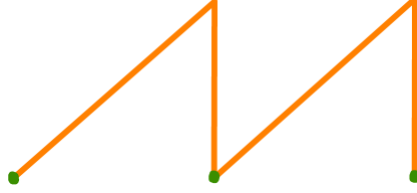


Figure 3.9: Modulus operation output waveform

From the triangular-like signal shown in Figure 3.9, a clock must be generated. For this purpose, a boolean relational operator has been used.

The domain of the remainder operation is $[0, 360^\circ/N]$. The principal clock characteristic is that at every exact sampling, an interruption (i.e. a rising edge) has to be generated. Thereby, assuming that the pPLL output is linear in steady-state, a clock falling edge must occur when the remainder operation is at its midpoint, as shown in Figure 3.10.

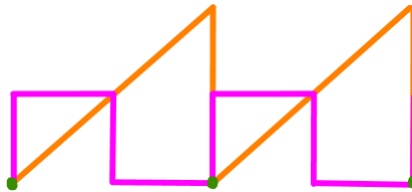


Figure 3.10: Generated software clock.

If the estimated frequency of the grid voltage is \hat{f} , by taking N samples per period, the generated clock will have a frequency of $N\hat{f}$. Notice that if interruptions are defined at both rising and falling edges, then modulating by $360^\circ/N$ will produce $2N$ samples per period. This latter approach is used for the simulations presented in Chapter 4 since it reduces the computational load. Full software clock generation block is shown in Figure 3.11 with simulation results in Figure 3.12.

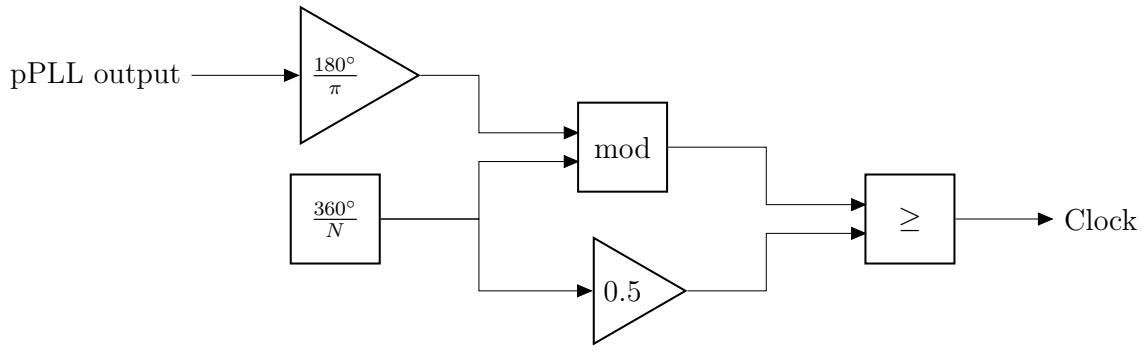


Figure 3.11: Software clock scheme.

The first-order LPF in Figure 3.11 was designed with a time constant of 20 ms.

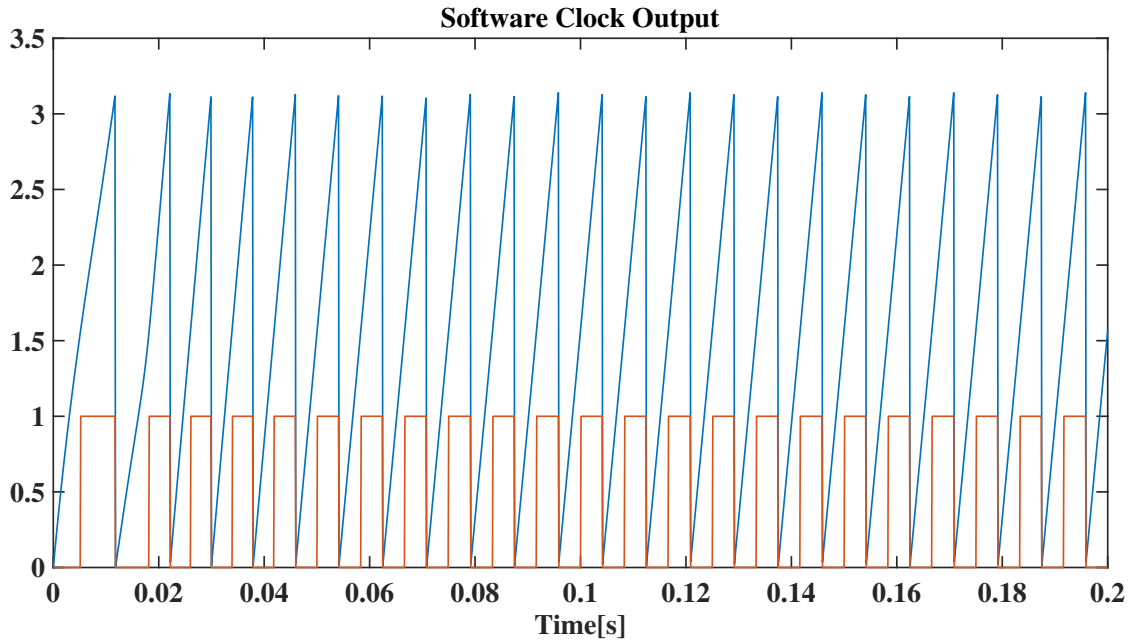


Figure 3.12: Simulation output of the software clock (in blue is shown the remainder output).

3.3.2 Hardware Interruptions

Software generated interruptions might not be good enough in implementation. That being so, a system for generating hardware CPU interruptions was also designed.

This system is based on the idea that the generated clock shall have a frequency $N\hat{f}$, \hat{f} being the estimated frequency by the pPLL. Since the number of samples per period N is given, the block diagram in Figure 3.13 essentially computes the actual frequency of the grid in order to

vary in a dynamic fashion the carrier period of a hardware PWM module. The duty cycle of the module has to be kept constant at 0.5. Results of implementation are presented in Chapter 4.

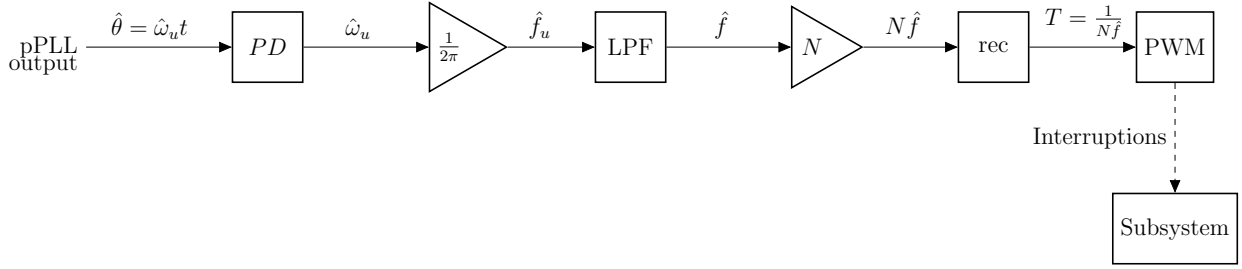


Figure 3.13: Hardware Interruptions scheme.

The PD filter was designed as a filtered derivative of order 2500 with the following transfer function:

$$PD[z] = \frac{2500z - 2500}{z - 0.75} \quad (3.30)$$

The LPF was designed in continuous time as a first-order filter with a time constant of 20 ms. It was discretized using the tustin method and a sample period of $T_s = 100 \times 10^{-6}$ s. The resulting discrete transfer function is:

$$LPF[z] = \frac{0.002494z + 0.002494}{z - 0.995} \quad (3.31)$$

3.4 Design of Controllers

3.4.1 Control Architecture

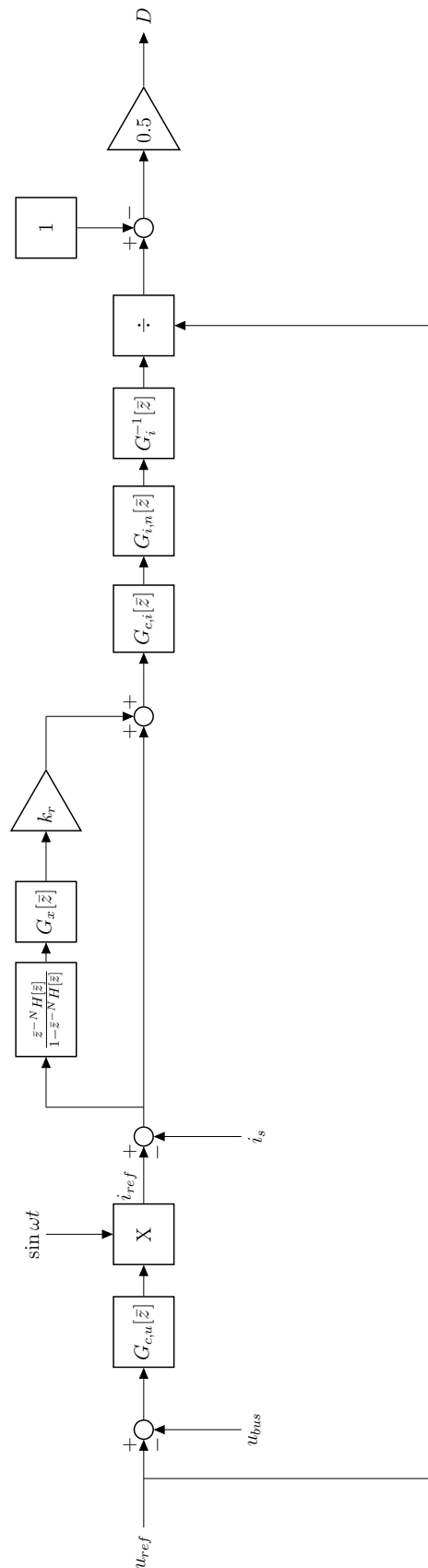


Figure 3.14: Control Architecture.

Figure 3.14 shows the proposed control architecture where:

Measurements

- u_{bus} : feedback from the DC bus voltage.
- $\sin \omega t$: normalized grid voltage.
- i_s : source current.

References

- u_{ref} : reference DC bus voltage.
- i_{ref} : reference current for the current loop.

Controllers

Recall that all controllers are expressed in angular space domain.

- $G_{c,u}[\bar{z}]$: voltage bus controller.
- $G_{c,i}[\bar{z}]$: current controller.
- $\frac{\bar{z}^{-N}H[\bar{z}]}{1-\bar{z}^{-N}H[\bar{z}]}$: internal model.
- $G_{i,n}[\bar{z}]$: nominal current plant.
- $G_i^{-1}[\bar{z}]$: inverse current plant.
- i_{ref} : control signal for the IGBTs.

Two control loops are designed: a voltage loop and a current loop. The voltage loop output gives the reference level for the current loop, in which angular space repetitive control is applied. After the current controller the inverse definition of α in Equation 3.1 is applied to compute the IGBT control signal D , from which the PWMs for the power electronics modules is computed.

Both controllers are designed from the continuous models of the plant using the corresponding transfer functions in angular space. Afterwards, they are discretized using the constant sample time in angular domain that yields 200 samples per period:

$$T_s = \frac{2\pi}{N} = \frac{\pi}{100} \quad (3.32)$$

3.4.2 Current Loop Controller

The current controller is designed in continuous angular space domain applying frequency-domain techniques. A phase-lead compensator is selected:

$$G_{c,i}(\bar{s}) = \frac{1 + bT_2\bar{s}}{1 + T_2\bar{s}} \quad (3.33)$$

For a phase margin of 110° , the resulting transfer function is:

$$G_{c,i}(\bar{s}) = -7.5 \frac{0.001814\bar{s} + 1}{0.0007642\bar{s} + 1} \quad (3.34)$$

The equation 3.34 is discretized with the angular space T_s of $\frac{2\pi}{200}$ by means of the tustin method to obtain:

$$G_c[\bar{z}] = \frac{-7.976\bar{z} - 6.657}{\bar{z} + 0.9511} \quad (3.35)$$

The resulting Bode Diagram is shown in Figure 3.15.

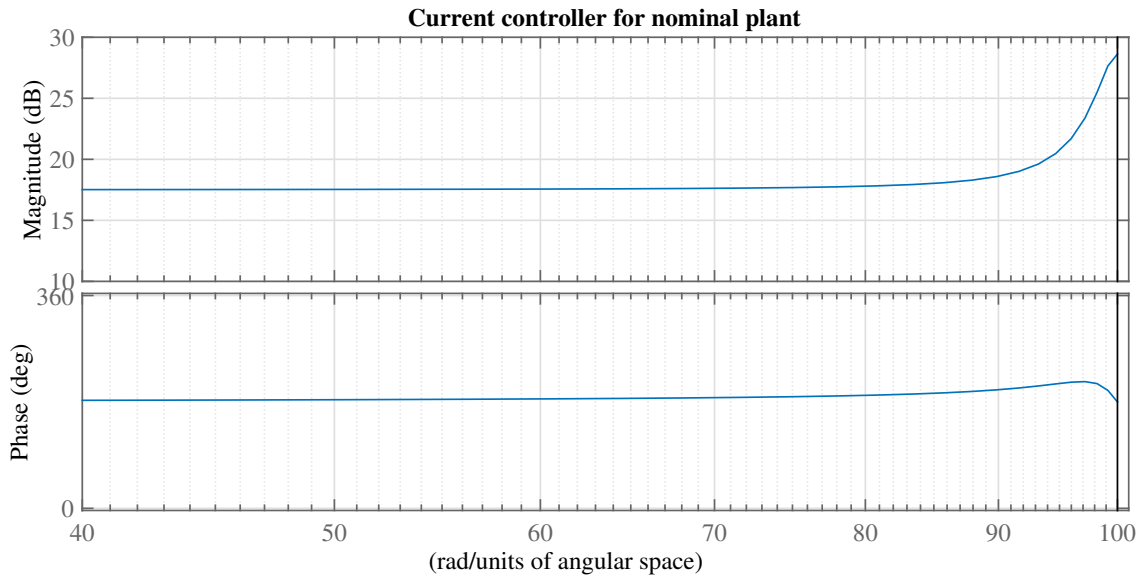


Figure 3.15: Bode Plot of the phase-lead compensator designed for the nominal plant.

The magnitude bode plot of controller, the nominal plant and the internal model is presented in Figure 3.16.

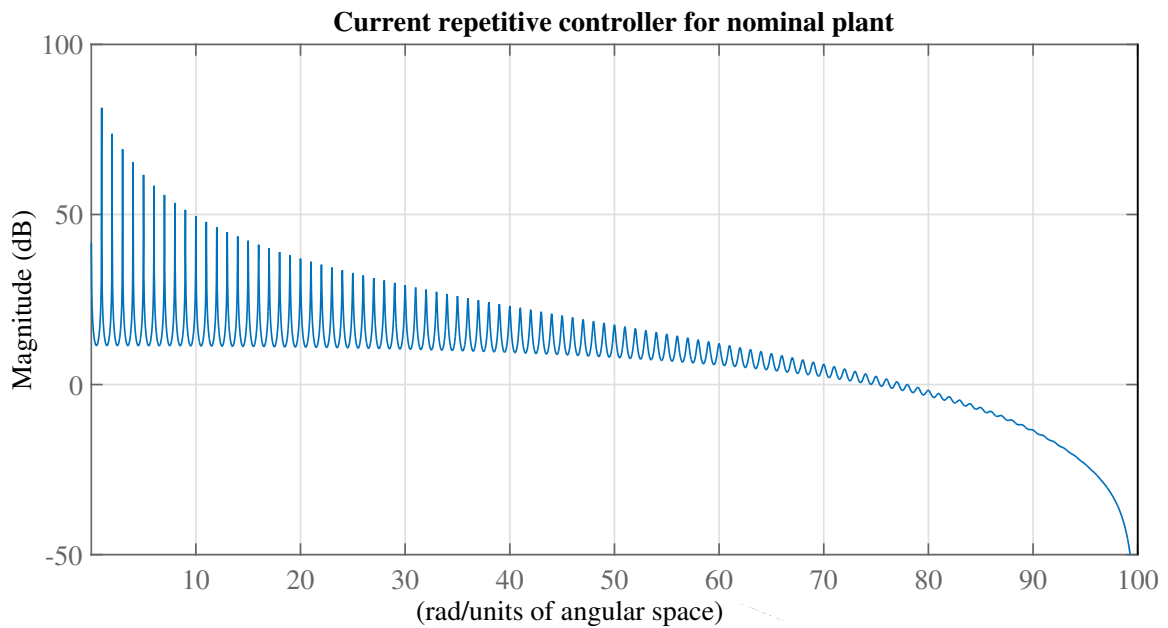


Figure 3.16: Magnitude bode plot of the main loop including controller and the internal model designed for the nominal plant.

The closed-loop Bode plot of the system including the nominal plant in angular space but omitting the internal model and the repetitive part is presented in Figure 3.17.

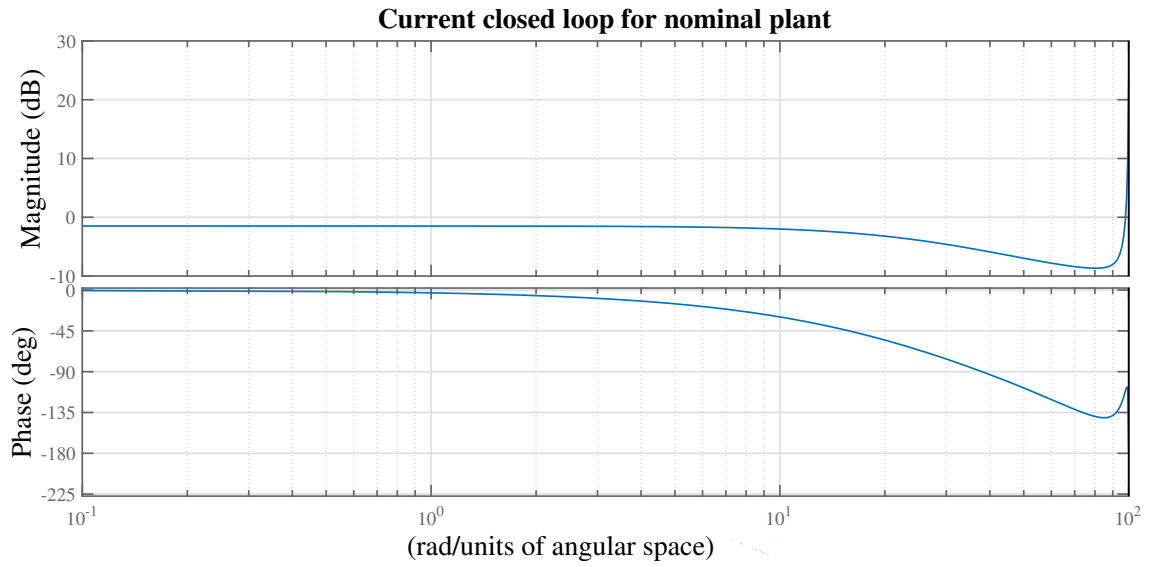


Figure 3.17: Bode plot of the closed-loop system without ASRC ($G_o[\bar{z}]$).

Figure 3.18 shows the Bode Plot of the closed-loop system including ASRC.

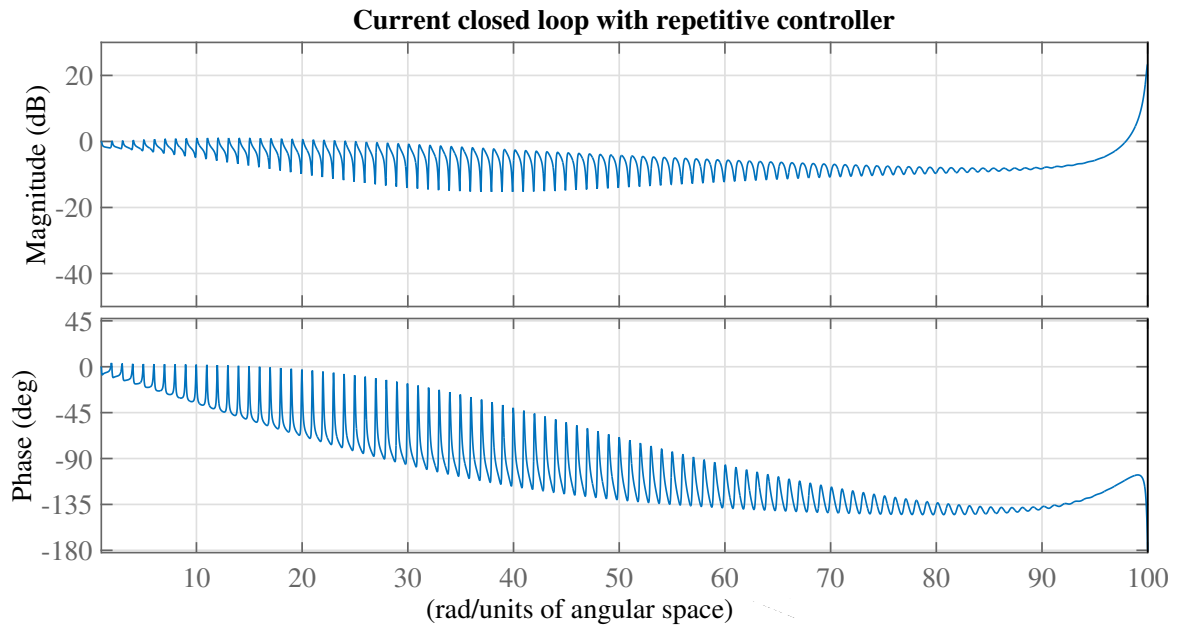


Figure 3.18: Bode plot of the closed-loop system with ASRC.

None of the previous Bode plots include the angular space plant precompensation.

The bandwidth of the current closed loop without repetitive structure shown in Figure 3.17 is 29.133 rad/units of angular space. For the current closed loop shown in Figure 3.18, the

bandwidth is 5.855 rad/units of angular space. Even though the bandwidth with the plug-in internal model is smaller, the introduced high-gain peaks significantly contribute to the rejection of the high-order harmonic disturbances in the control loop.

It also has to be mentioned that the H-filter has to be designed after physical implementation of the system. For the simulation case, after iteration, the following filter has been selected:

$$H[\bar{z}] = 0.25\bar{z}^{-1} + 0.5 + 0.25\bar{z} \quad (3.36)$$

3.4.3 Voltage Loop Controller

The voltage loop is designed in standard control configuration with unity negative feedback. Since no periodic signal is to be followed, repetitive control is not applied. A DC bus voltage of 60 V is selected taking into account that the source voltage will be at 40 V peak, as discussed in Chapter 4.

According to [23], in order to avoid voltage fluctuations on the DC bus, the transient of the response has to be slow. In the words of [22], the variation of the voltage in the DC bus during a period has to be small enough compared to the current DC bus voltage. As done with the current controller, a frequency-domain technique is selected to tune the selected PI controller. The bandwidth of the resulting system is set so that it will be at least 10 times slower in comparison with the current loop ¹. In this way, the voltage loop might be seen as constant from the perspective of the current loop. Thus, this kind of "separability" enables to perform an independent design for each system section.

$$G_{c,u}(\bar{s}) = k_p + \frac{k_i}{\bar{s}} \quad (3.37)$$

After tuning, the obtained compensator is:

¹In [17] a bandwidth 5 times slower is chosen

$$G_{c,u}(\bar{s}) = 0.2 + \frac{0.004}{\bar{s}} \quad (3.38)$$

After discretizing with a sampling time of T_s of $\frac{2\pi}{200}$ by the tustin method, the compensator in discrete angular space domain is:

$$G_{c,u}[\bar{z}] = \frac{0.2001\bar{z} - 0.1999}{\bar{z} - 1} \quad (3.39)$$

The equation 3.39 is discretized with the angular space

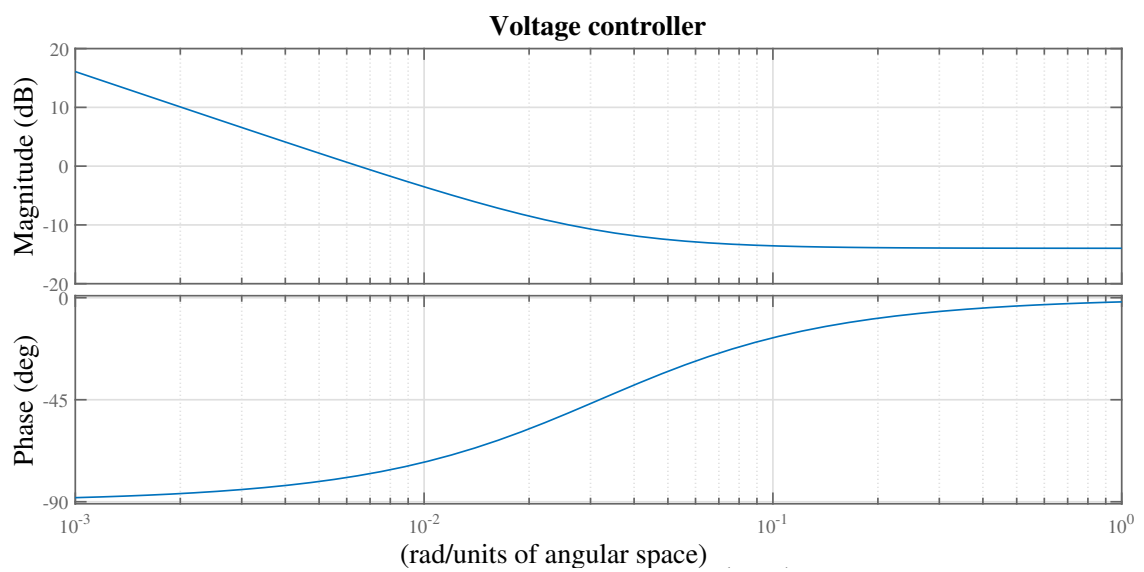


Figure 3.19: Bode plot of the PI controller for the voltage loop.

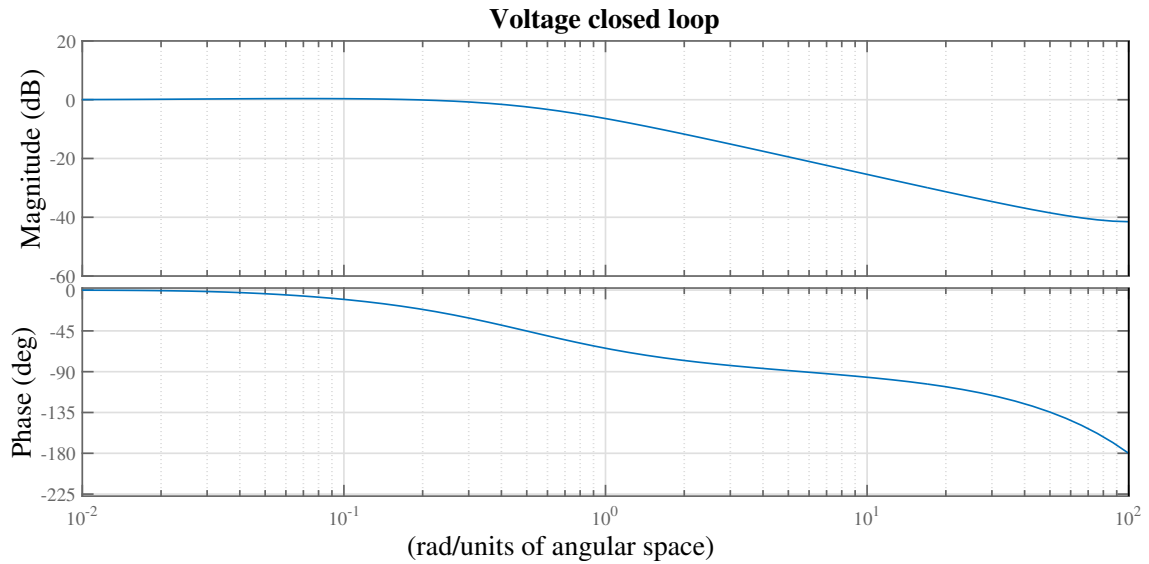


Figure 3.20: Bode plot of the closed-loop voltage controller.

The bandwidth of the current closed loop shown in Figure 3.20 is 0.5654 rad/units of angular space this obeys the design criteria that says that the voltage loop should be at least ten times slower than the current loop. It may also be highlighted that despite the H -filter attenuation, the RC gains also have an effect at high frequencies.

Chapter 4

Simulation and Implementation

First, the implementation of the pPLL-based hardware interruption testing platform is detailed, in which a DSP from Texas Instruments has been used (F28335). Subsequently, the Simulink model for the whole system is presented. Simulation results for RC and ASRC under variable-frequency scenarios are both compared and analyzed ¹.

4.1 Implementation of Testing Platform

4.1.1 Texas Instruments F28335 Delfino

The Texas Instruments Experimenter's Kit (TMS320C28335) is used for this implementation. This device offers various advantages but the most important ones are:

- 32-Bit CPU single-precision floating point with high-performance up to 150 MHz;
- its docking station that facilitates the USB-JTAG connection and offers a header pin access to key MCU signals.

¹It is recommended to use MATLAB R2015a or a previous release for recreating the simulations described in this Chapter

In summary, this device offers an optimal platform to implement the testing platform required by the angular space repetitive controller.

4.1.2 SolidThinking Embed 2016 - VisSim Embedded

SolidThinking a visual environment that eases the design and debug of models to be implemented on embedded systems. It offers blocks for building processes together with a high efficient C-code compilation.

The implementation of the testing-platform system is represented in the Figure 4.1, where three blocks are shown:

- the first one represents the configuration of the target device where the program will be run;
- the second block contains the pPLL system. It runs with a local time step of 0.001 seconds that corresponds to the sample time of the discretization of the already known pPLL. Besides of that, this block runs in a background thread, giving priority to the third block, which contains the controller system.

The system will be executed on a hardware signal interrupt sent by a PWM, whose carrier period is controlled by the output frequency of the pPLL system.



Figure 4.1: General system on VisSim Embedded.

This interrupt signal is sent in the center of the low state of the PWM. To demonstrate this, the simple system in Figure 4.2 was implemented. It works as a clock that changes depending on the new calculated states at every interruption.

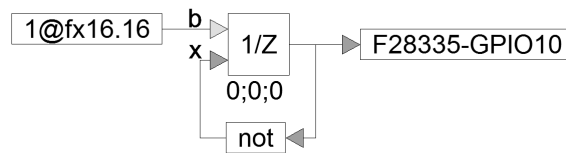


Figure 4.2: Test system for the understanding of the interrupt signal.

Three different sinusoidal waves are used as input to the PLL system, the calculated frequency is multiplied 200 times, representing 200 samples per period. After that, the outputs are visualized in an oscilloscope. The upper signal is the PWM controlled by the PLL and the lower one is the output of the system that should have the half of the frequency.

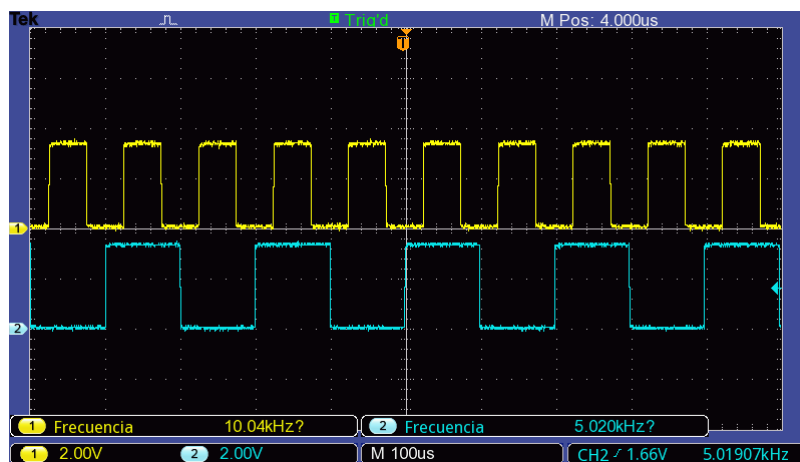


Figure 4.3: Output of the test system with input of sinusoidal wave of 50 Hz.

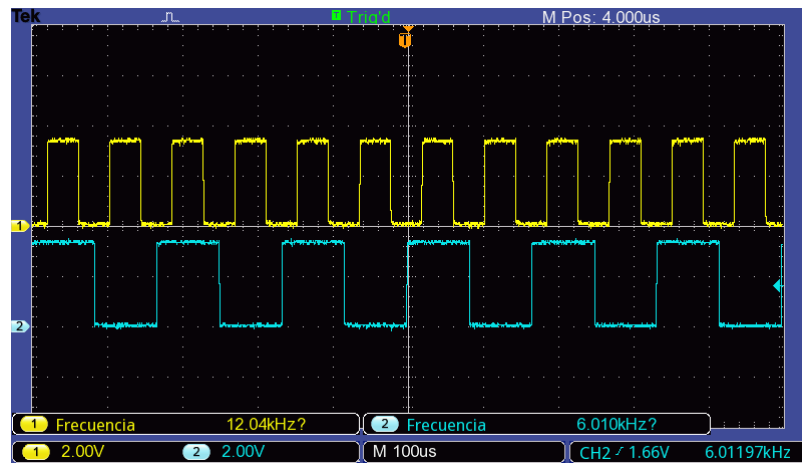


Figure 4.4: Output of the test system with input of sinusoidal wave of 60 Hz.

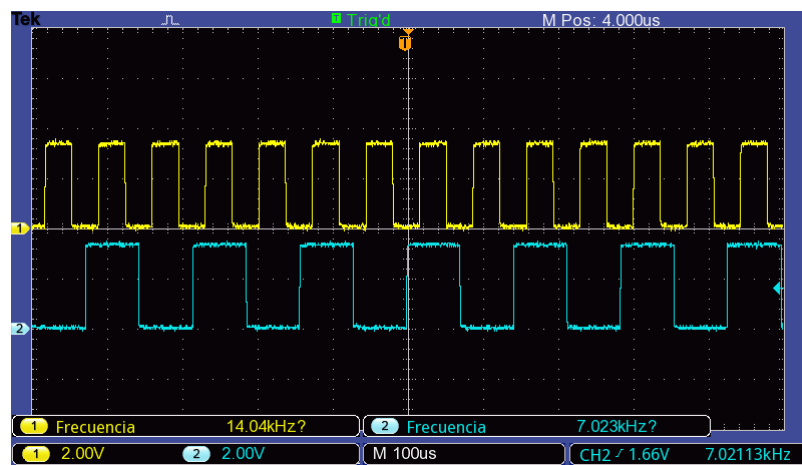


Figure 4.5: Output of the test system with input of sinusoidal wave of 70 Hz.

4.2 Simulink Simulations

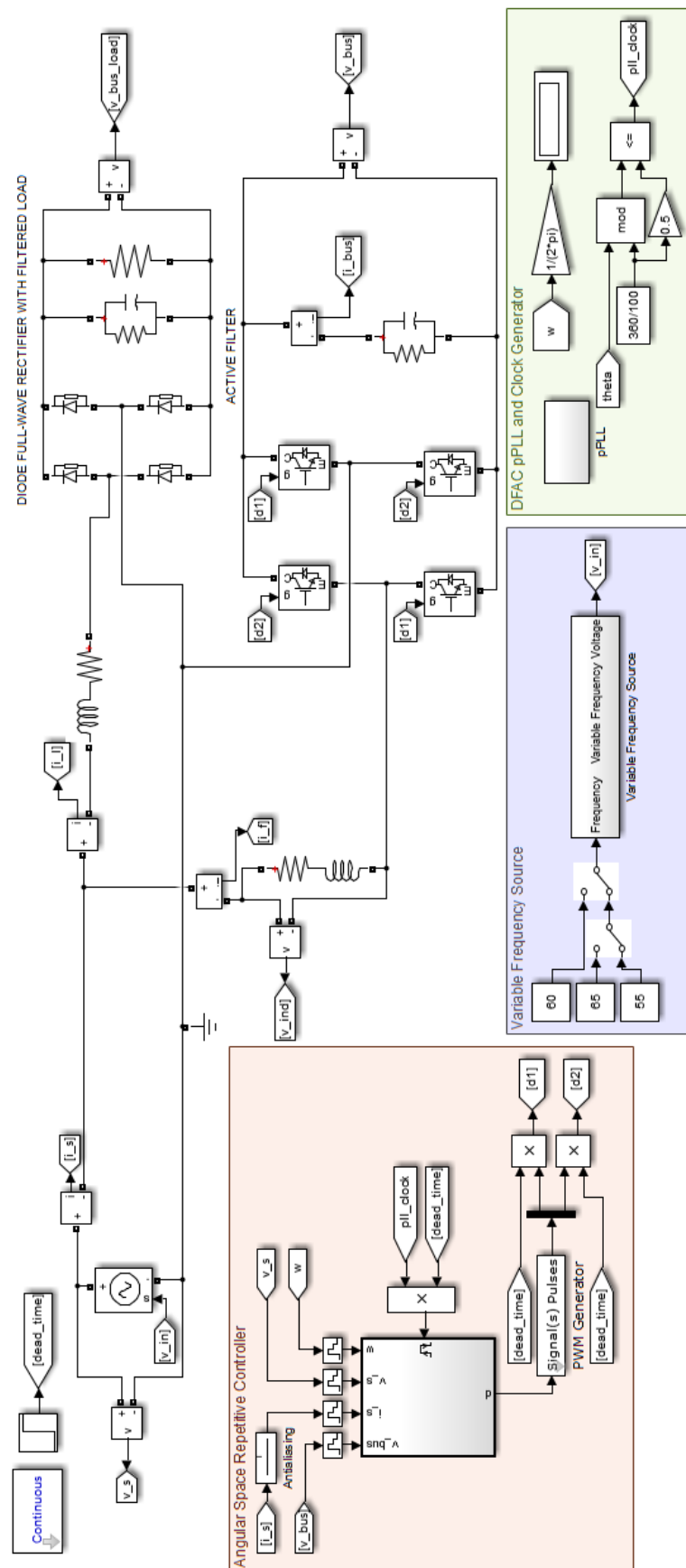


Figure 4.6: Simulated Simulink model

Figure 4.6 shows the Simulink model of the complete system.

There are a couple of details about the configuration of the Simulink model and the parameters of the solver with which the simulation was executed:

- The solver step time runs 50 times faster than zero-order hold blocks sampling-time placed before the input of the angular space repetitive controller (and the repetitive controller). These sampling time was defined as $\frac{1}{12000}$ s.
- To avoid signal deformation by the sampling process, a first-order anti-aliasing filter with cut frequency of 4500 Hz has been deployed before A/D conversion [26, p. 465-467].
- For the calculation of the THD, a first-order LPF is also implemented with a cut frequency of 2200 Hz, having in mind the Electrical Multifunction Analyzer ANR96 of ABB, which employs the first 31 harmonics of the input signal for the THD calculation.
- The implemented dead time intends to give time to the pPLL to settle and to the DC Bus capacitor to charge, so that the rush-in current will not result too high.

4.2.1 Dynamic pPLL Analysis

Since the pPLL itself is a closed-loop system, the study of its dynamics is important to ensure the proper operation of the control system which should start when the pPLL reaches steady-state.

For this purpose, the output of the pPLL was studied with three frequency changes at 0.5 s and 1.5 s. Results are plotted in Figure 4.7.

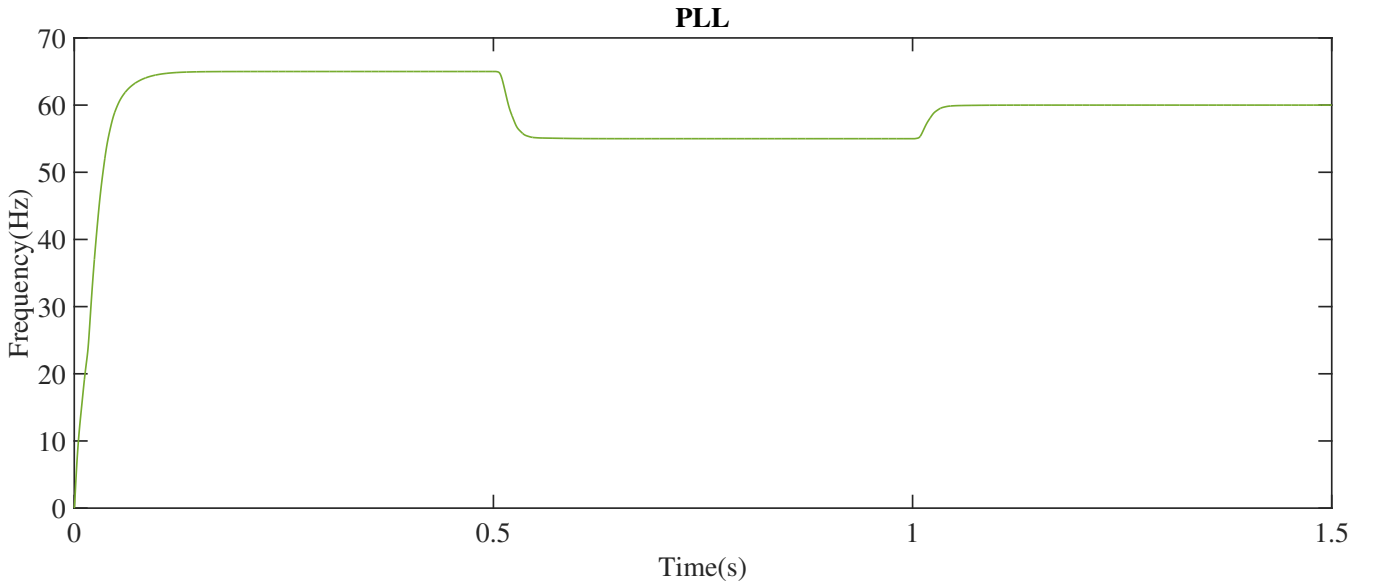


Figure 4.7: Simulation of pPLL dynamics.

The settling-time of PLL depends on the initial value of the grid frequency. To detail its behavior, different combinations of frequency changes were tested. Obtained values are gathered in Table 4.1.

65-55-60		60-55-65		55-60-65	
Time (s)	Frequency (Hz)	Time (s)	Frequency (Hz)	Time (s)	Frequency (Hz)
0.1922 s	55 Hz	0.1881 s	65 Hz	0.1873 s	60 Hz
0.1579 s	60 Hz	0.1232 s	55 Hz	0.1560 s	55 Hz
0.1140 s	65 Hz	0.1150 s	60 Hz	0.1290 s	65 Hz

Table 4.1: Settling time of the pPLL for different combinations of frequencies.

Taking into account these results, a dead time of 0.15 s is defined, after which the controller will be enabled. The output frequency at this time is:

- 54.97 Hz at 55 Hz.
- 59.96 Hz at 60 Hz.
- 64.96 Hz at 65 Hz.

This value is good enough to compute the required interruptions and execute angular space control algorithms.

4.2.2 Repetitive Controller Simulation

For a better visualization of the difficulty of controlling a system with grid frequency deviations, a controller with a repetitive structure designed for 60 Hz was first simulated. Simulink model is similar to that shown in Figure 4.6 without the pPLL-based platform. For the voltage loop, a PI controller has been tuned.

The magnitude of the variable-frequency source voltage of the system is set as 40 V peak, initially at 60 Hz. After a dead time, enough to let the DC Bus capacitor to charge, the controller is activated. In 0.4 s, the source frequency is changed to 65 Hz, and in 0.7 s, to 55 Hz. Figure 4.8 shows the corresponding results for source, filter and load current.

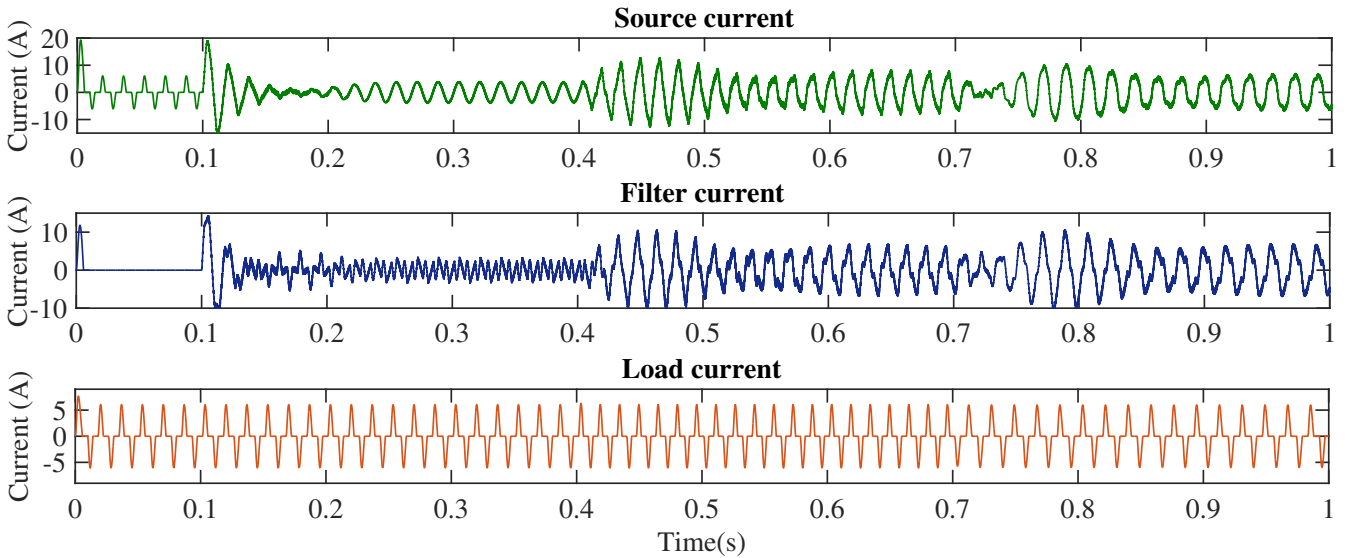


Figure 4.8: Currents of the system controlled by a repetitive controller design for 60 Hz with frequency changes at 0.4 and 0.7 s.

Notice that the tracking of the sinusoidal reference is not achieved neither for 65 Hz nor for 55 Hz as is done for 60 Hz. This puts in evidence the performance drawbacks of the RC in variable-frequency conditions.

One could clearly appreciate in Figures 4.8 and 4.9 that, even though RC does not achieve asymptotic tracking of the sine current reference, it is capable of neglecting a considerable number of harmonics in steady-state for 55 and 65 Hz. Also, the settling-time for 60 Hz is around 0.255 s.

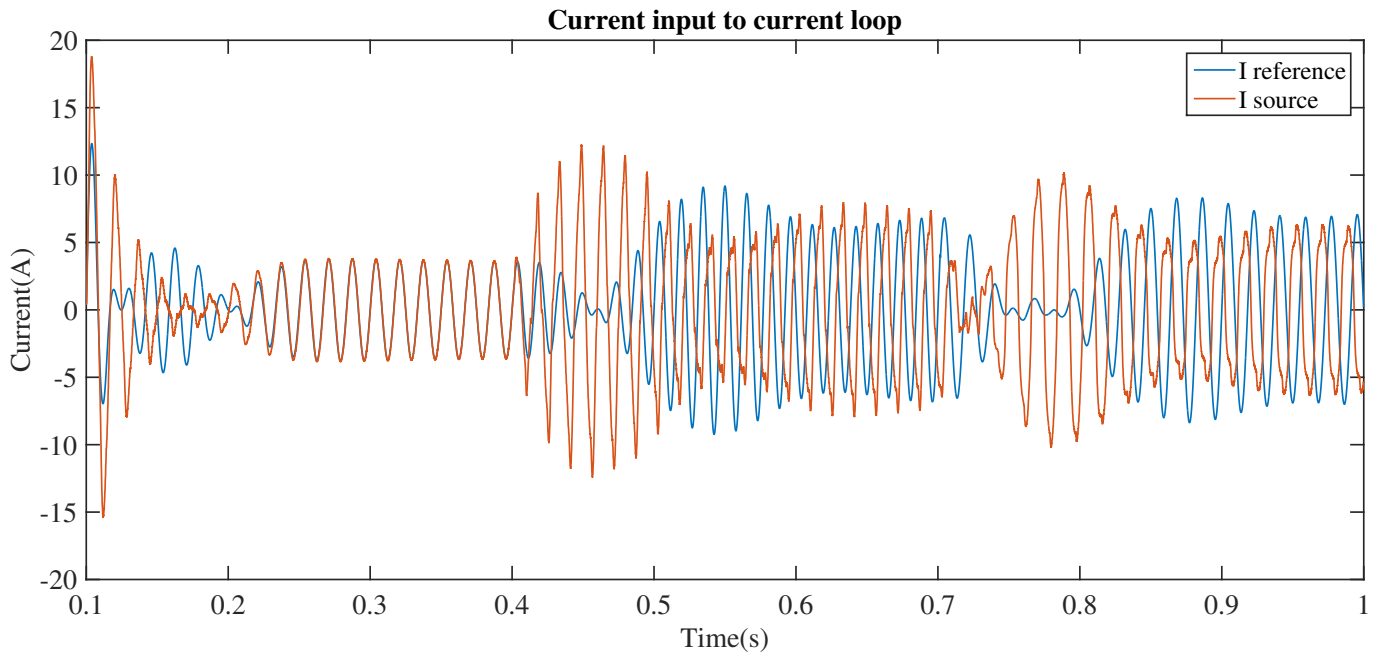


Figure 4.9: Tracking of the reference current by the RC current control loop.

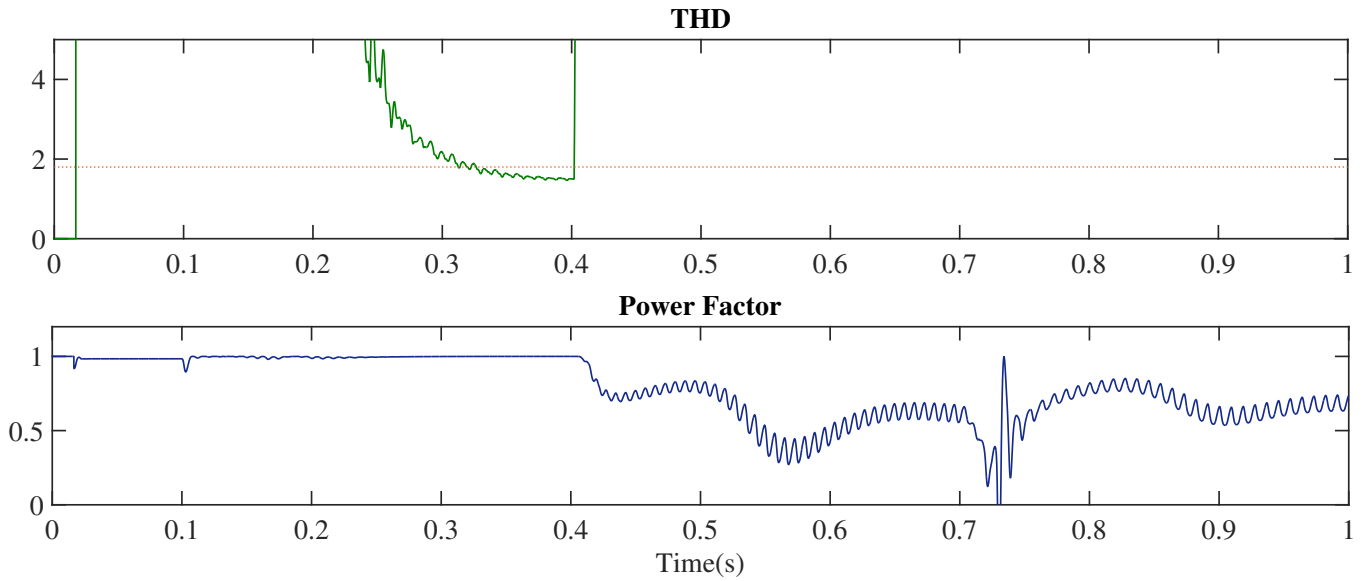


Figure 4.10: THD and Power Factor of the source with a RC current control loop.

In Figure 4.10 one sees that, even though the settling time seems to be around 0.255 s, the THD does not go better so quickly. It is just until 0.32 s that goes lower than 1.8%. For the other frequencies, the figure does not show the values because they are really above a useful or meaningful value. For 55 and 65 Hz, however, the steady-state THD is around 16%.

4.2.3 Angular Space Repetitive Controller Simulation

Model of Figure 4.6 has been simulated with the control architecture shown in Chapter 3, using a PI discrete controller for the voltage loop and a ASRC topology for the current loop. The simulated controllers design was presented in Chapter 3.

A variable-frequency scenario with an initial frequency of 65 Hz, with prior changes to 55 (0.5 s) and 60 Hz (1 s) respectively, is shown in Figure 4.11.

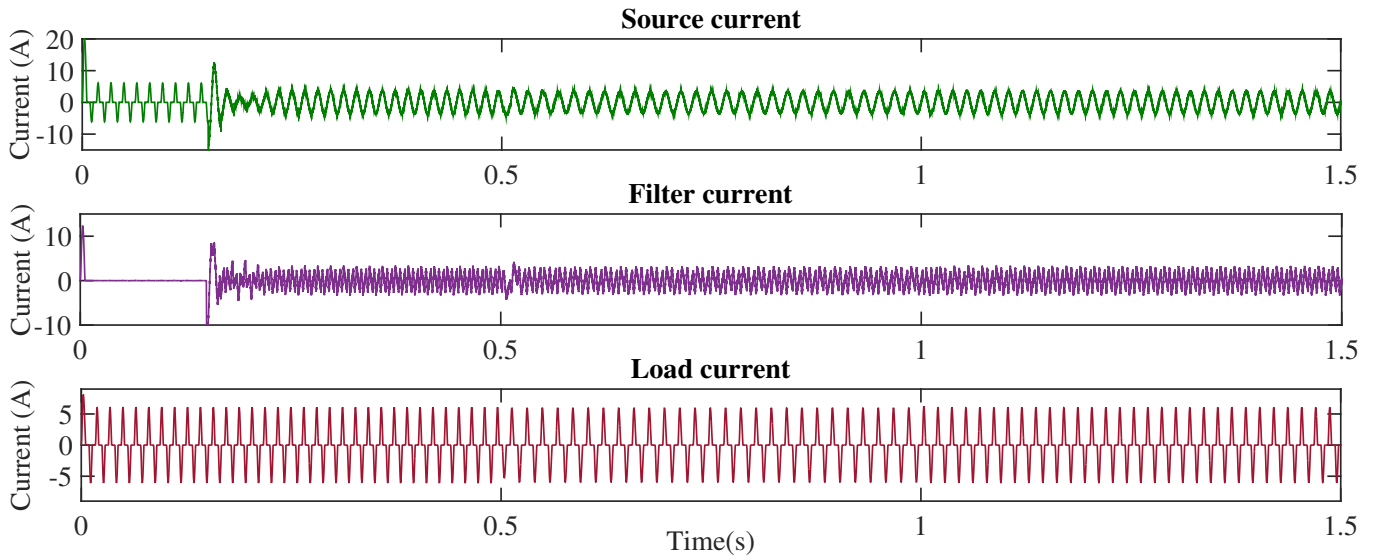


Figure 4.11: Currents of the system at variable-frequency scenario 65-55-60 Hz for ASRC.

Notice that the system is capable of asymptotically tracking the sinusoidal references. Also, the transient response is smoother than in the RC case.

From Figure 4.12 the settling-times of the source current for every frequency change in the simulation are calculated. When the signal is 65Hz, that means, the first established frequency, the settling time is 0.139 s. For the second frequency of 55 Hz, is 0.166 seconds; and for third frequency of 60Hz, is 0.130 s (Figure 4.2).

65-55-60	
Frequency (Hz)	Settling-time (s)
65 Hz	0.139 s
55 Hz	0.166 s
60 Hz	0.130 s

Table 4.2: Settling-time of the ASRC for the simulated frequency scenario.

Figure 4.12 shows the plot of the reference versus the source current as the error of the current control loop. In any case, the system tracks the sinusoidal signal in steady-state, independent of its frequency.

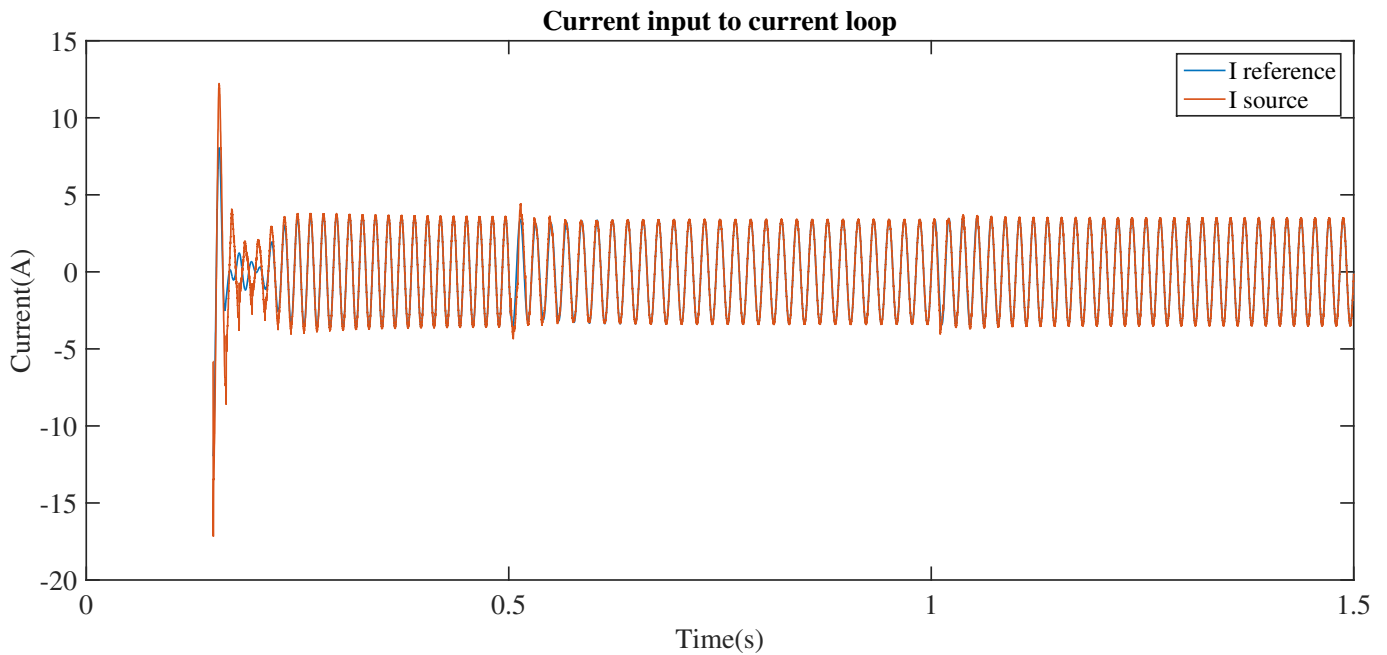


Figure 4.12: Tracking of the reference current coming from the outer voltage loop by the source current

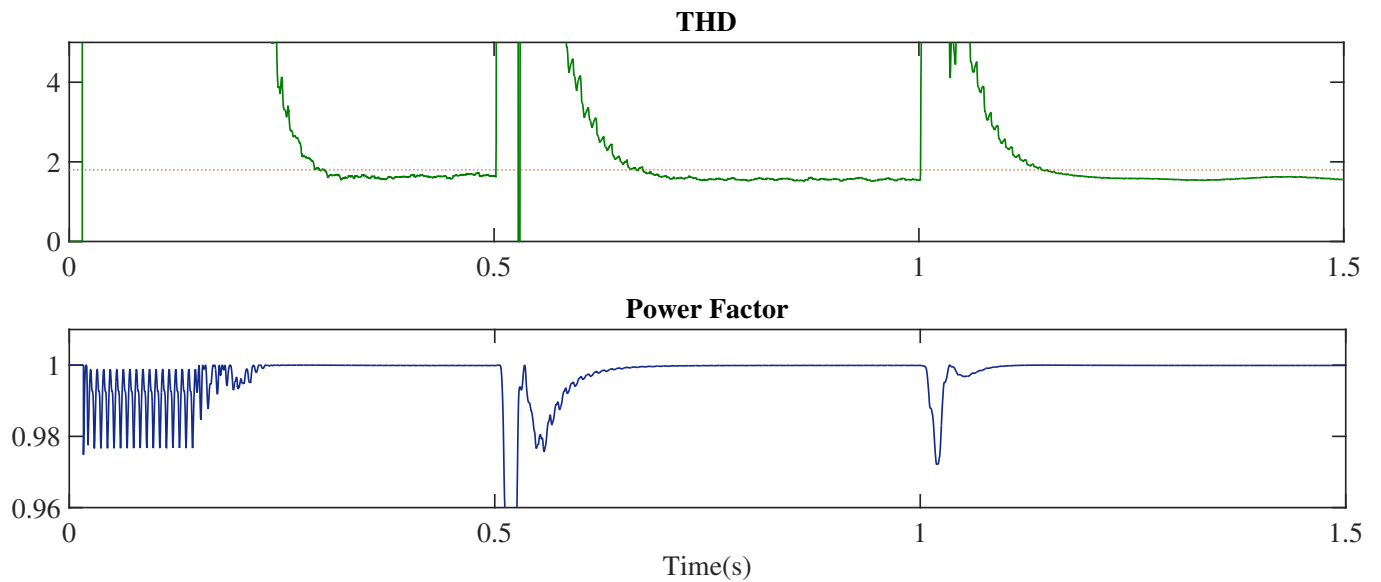


Figure 4.13: THD of the source and Power Factor from the source side.

Two important figures of merit of a APF are the THD and the power factor seen from the source side, shown in Figure 4.13. At the first frequency, the THD has a stationary value of

1.8%, whereas for the other two frequency cases it goes down to 1.5 and 1.6% respectively.

Another important response of the whole control system is the filter DC voltage bus. Recall that the reference for the voltage loop was 60 V. Figures 4.14 and 4.15 show the output for the voltage and current loops, respectively. It is clear that the voltage loop is much more slower than the current loop, as required in the design stage.

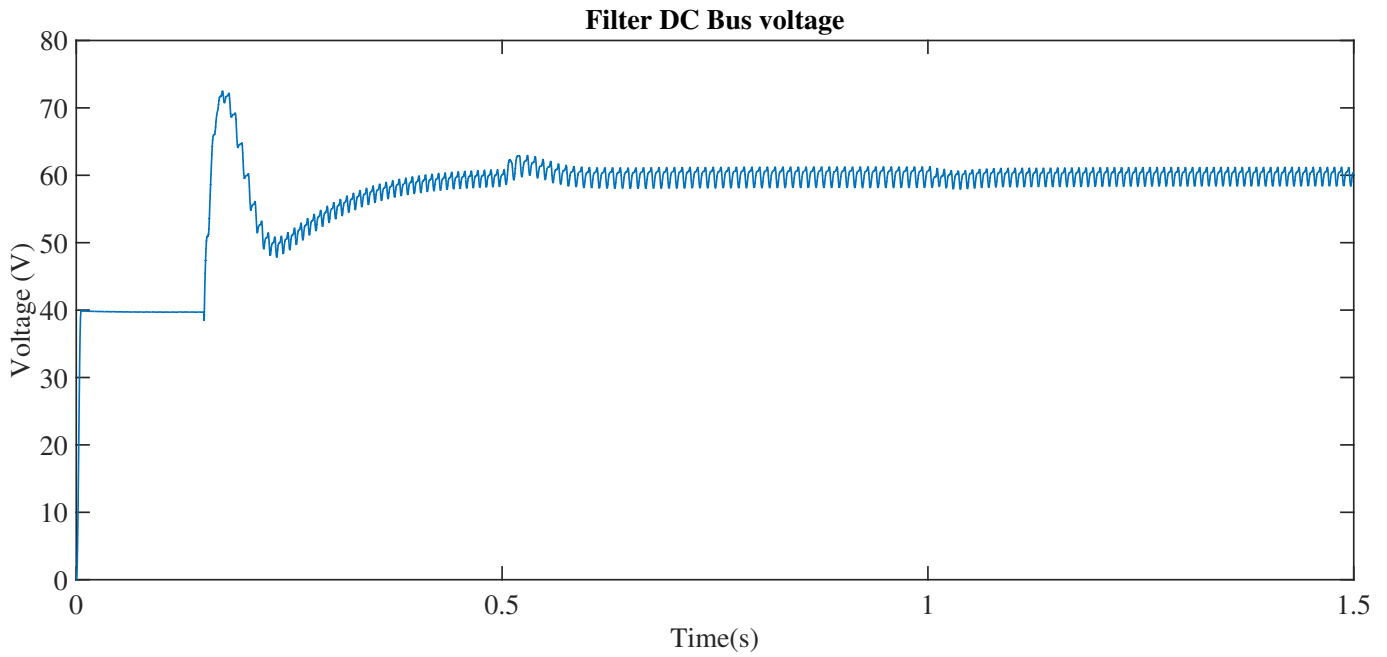


Figure 4.14: Voltage in the DC Bus capacitor

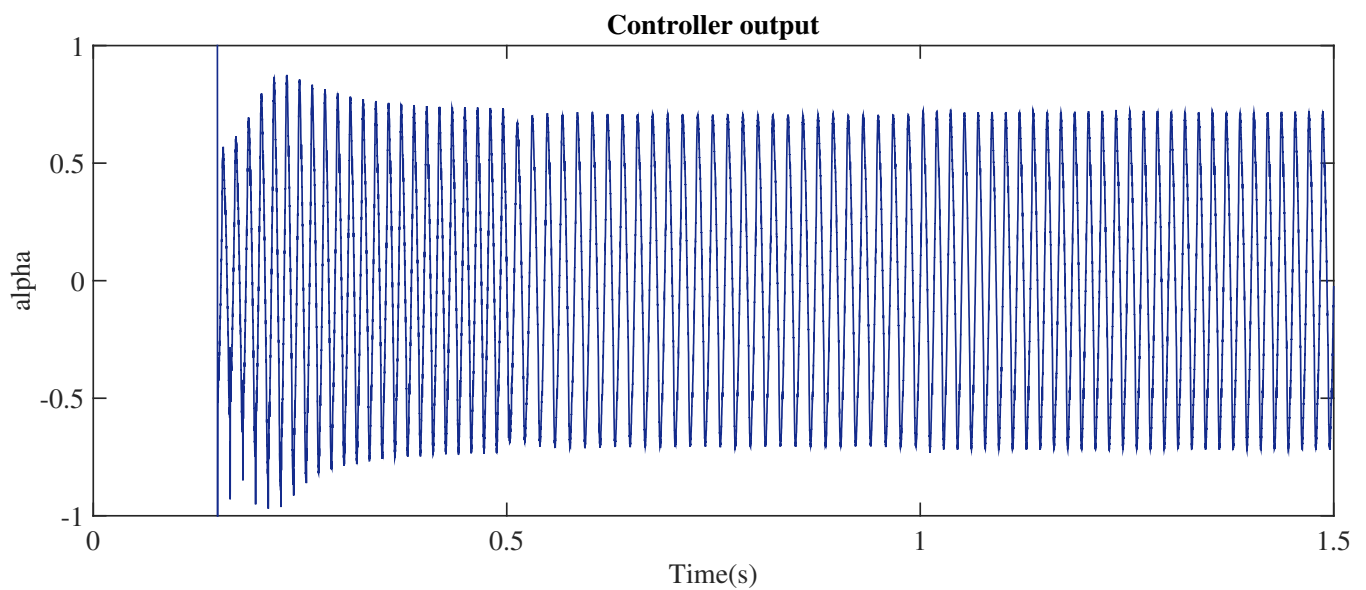


Figure 4.15: Controller output

Another couple of significant simulations are the ones where one can see the performance of the system at the boundaries of the frequency range of the European Standard EN50160. Because the nominal frequency in Colombia is 60 Hz, this 15% variation corresponds to the extreme values 50 and 70 Hz. A good sight is given by the Figures 4.16 and 4.17 where one sees that the settling time is around 0.31 seconds and the Figures 4.18 and 4.19 where the settling time is around 0.26 seconds.

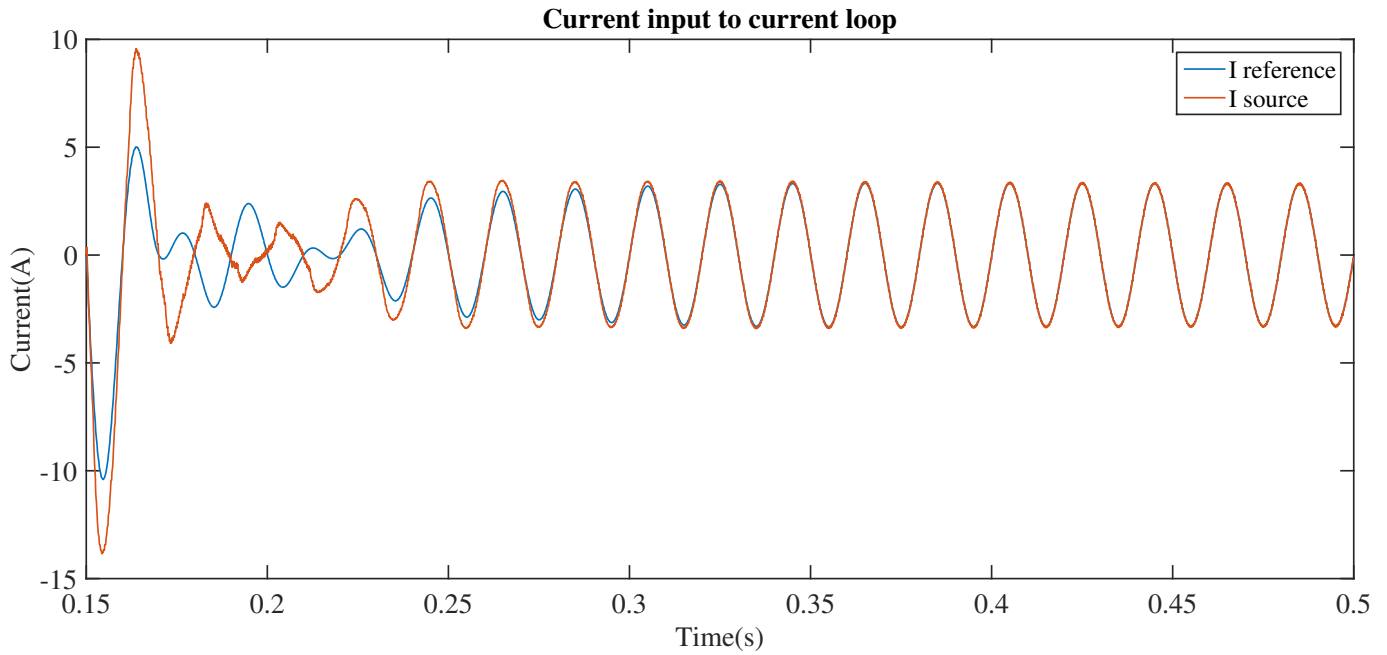


Figure 4.16: Tracking of a reference of 50Hz

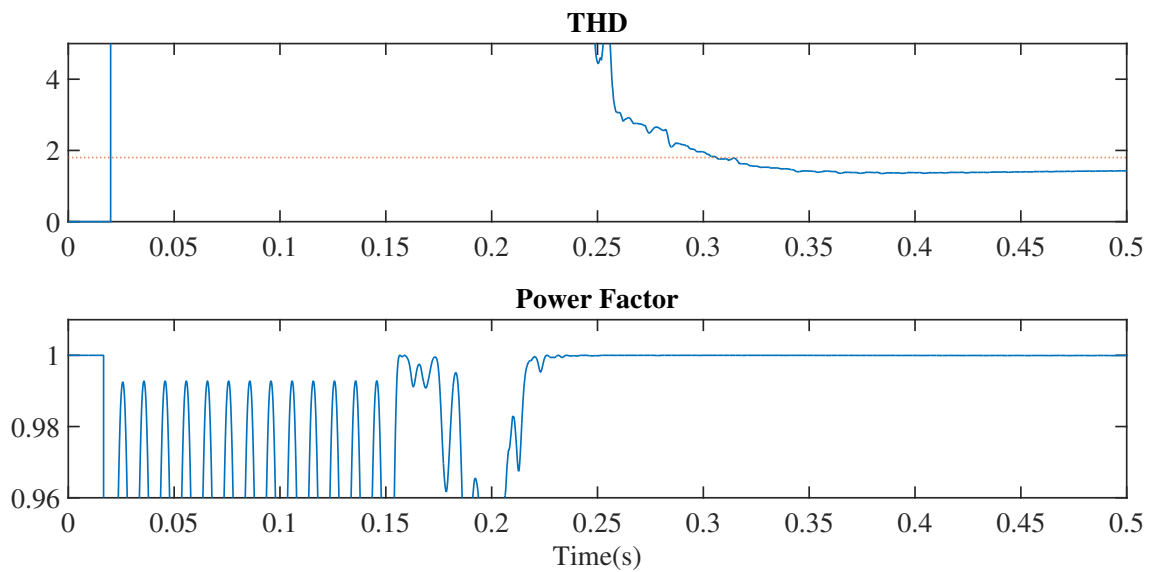


Figure 4.17: THD of the source current and Power Factor from the source side.

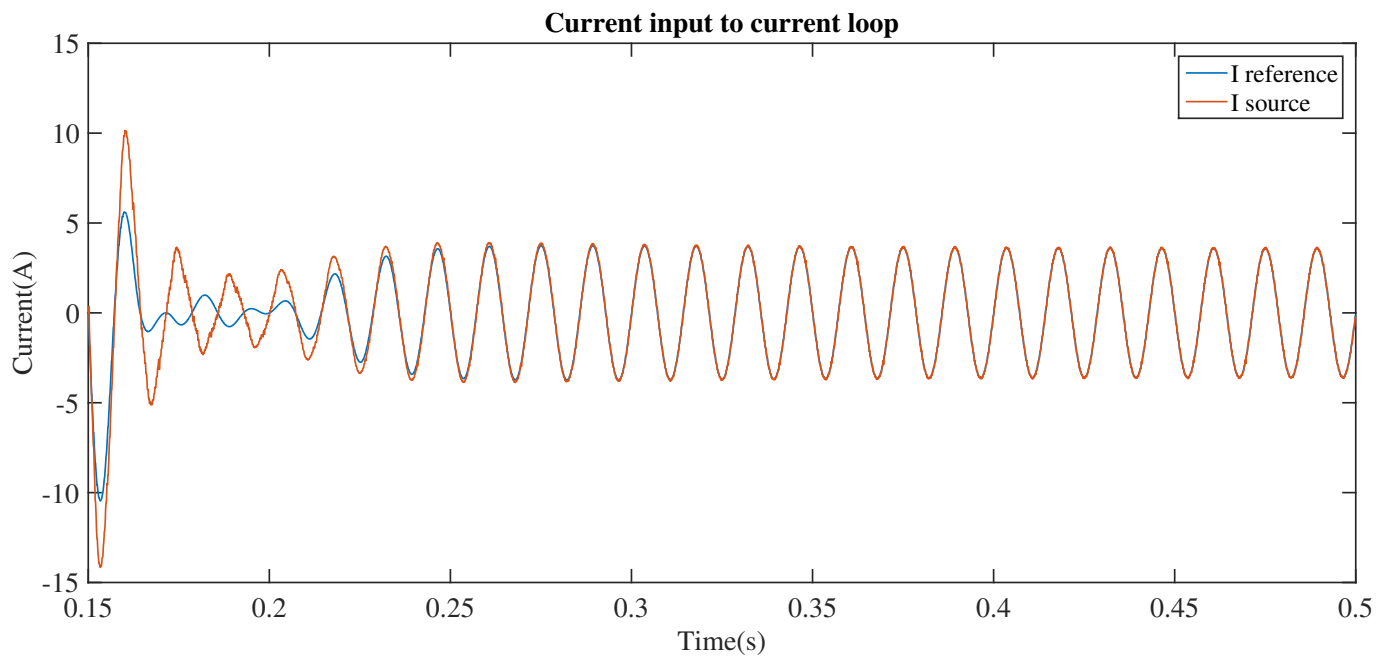


Figure 4.18: Tracking of a reference of 70Hz

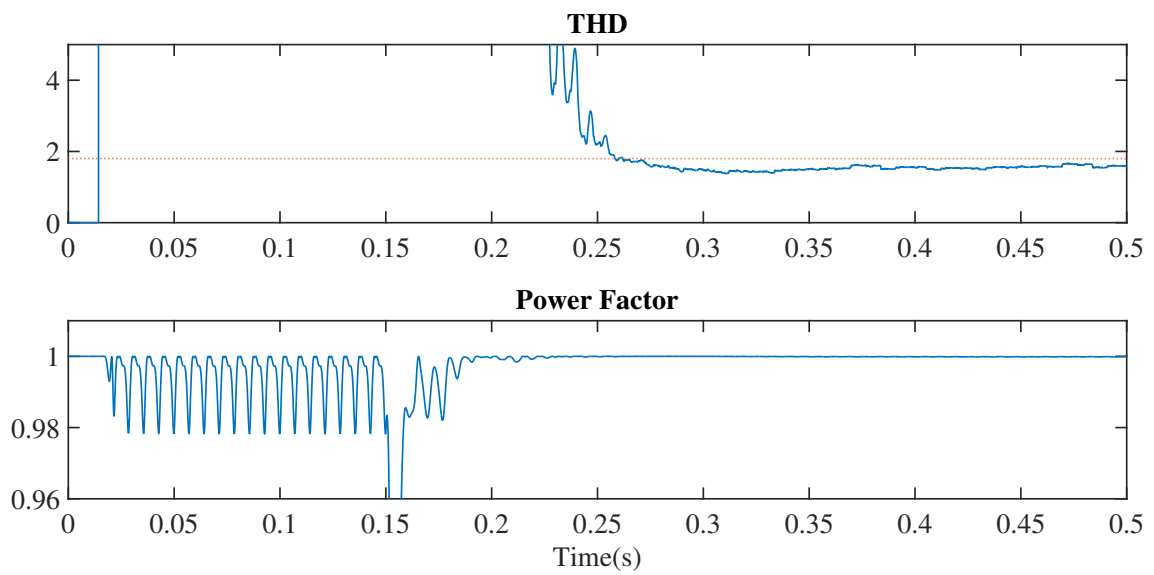


Figure 4.19: THD of the source current and Power Factor from the source side.

The changes in the voltage do not affect strongly the performance of the system in the way that it is still capable of tracking very well the reference as shown in the Figure 4.20. Also, it is called to mind that the DFAC pPLL has been designed for well operation in voltage changing conditions [24]. The effect of voltage changes from 40 V to 30 and 50 V is shown in Figures 4.20 and 4.21.

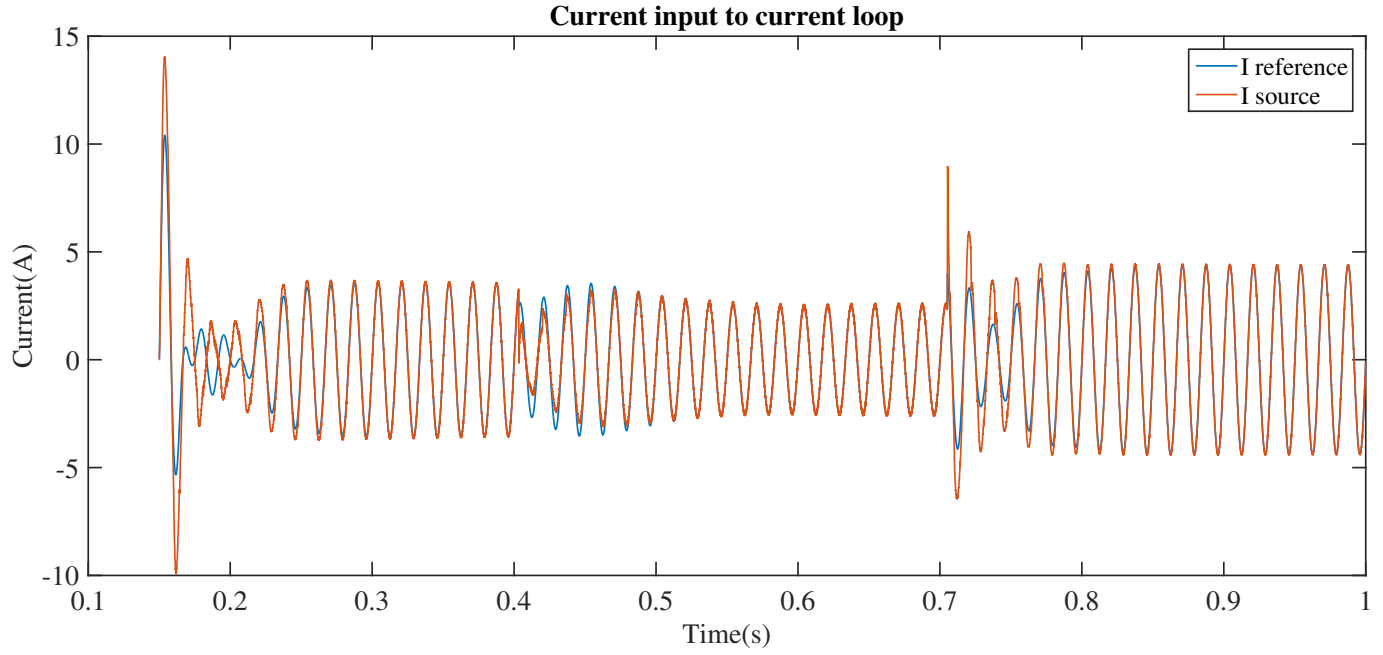


Figure 4.20: reference current and source current with variations of the voltage source amplitude

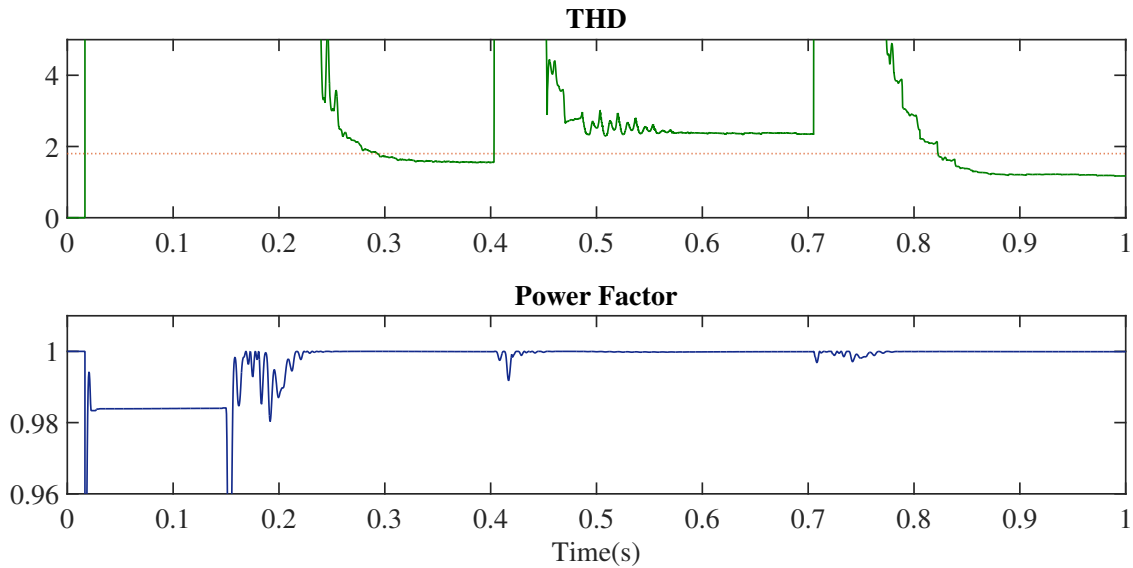


Figure 4.21: THD and PF of the source with variations of the voltage source amplitude

The system is capable of asymptotic tracking sinusoidal references. Nonetheless, grid voltage

variations affect the THD values as one can see in Figure 4.21 and Table 4.3.

65-55-60	
Peak Voltage (V)	THD (%)
30 V	2.3%
40 V	1.6%
50 V	1.2%

Table 4.3: THD variation with changes of the source voltage.

This should be due to the corresponding change of amplitude of the current signal reference which is normalized for a 40 V value. Hence, a dynamical normalization has been included into the signal processing blocks for system measurements so that the current reference shall always be computed from a unit amplitude sinusoidal signal at the frequency of the source. When the amplitude is either larger or smaller than 1, the switching ripple becomes more influent for the THD calculation.

Chapter 5

Conclusion

- The combination of the Internal Model Principle (IMP)-based Repetitive Control (RC) with the angular space transformation can be applied in order to overcome the performance withdrawals of RC when the frequency of the signal to be tracked varies with time.
- A simulation platform has been designed for the implementation of an Angular Space Repetitive Control (ASRC) system in an Active Power Filter (APF), and is based on a Power-Based Phase-Locked Loop (pPLL) that takes advantage of the Double Frequency cancellation and Amplitude Compensation (DFAC) scheme. The pPLL platform was tested using a Texas Instruments DSP (F28335). The designed module enables the generation of interruptions, which ensure that the number of samples per period taken by the control system is always the same, independent of the grid frequency. Tests have shown good behaviour for both software and hardware approaches. The device was programmed using SolidThinking Embed.
- The dynamics of the pPLL-based platform were considered to set a dead time before the starting of the system. The platform was found to respond dynamically faster after reaching steady-state from the first time.
- The main control requirements were to make the current source to track a sinusoidal

reference so that the power factor from the source side resulted 1. To achieve this purpose, two control loops have been proposed within the control architecture: one for the dc voltage and the another for the source current. The voltage bus controller was a PI controller in discrete angular space domain. The current controller has applied repetitive controller in angular space together with a plant precompensation technique to guarantee both tracking of sinusoidal references and rejection of undesired harmonics. Design of both controllers was carried out by frequency methods in angular space continuous Laplace domain. Afterwards, they have been discretized using the tustin method and a fixed sample time in angular space domain.

- Using Simulink, simulations for both repetitive and angular space repetitive control systems have been carried out at different frequency scenarios. RC has been shown to downgrade its performance when subjected to a frequency other than nominal.
- ASRC architecture has performed according to requirements in steady-state in different variable-frequency scenarios so that the frequency deviations covered the percentage stated in the European Standard EN50160 for operation of low inertial microgrids in islanding mode: $f_n \pm 15\%$. For 60 Hz, the frequency range lies between 50 and 70 Hz, in which the ASRC has functioned correctly.
- A module for normalizing the amplitude of the grid voltage measurement has to be programmed for the execution of the algorithm in a DSP. Even when the pPLL compensates voltage amplitude changes, such variations have been shown to have an influence when the current reference is calculated and the controller performance is therefore modified.
- THD has been used as an indicator for the performance of each simulation. In spite of that, the values reported in this document shall not be compared to those reported in scientific literature from experimental results because simulations permit abrupt changes in the current due to switching to happen. An antialiasing filter and a low-pass filter were thereby deployed in order to emulate in a better way the behavior of a practical measurement instrument for the computation of the THD.

5.1 Future Work

In order to avoid grounding problems and electrically isolate the power from the measurement circuit, authors suggest to use the following sensing devices for the physical implementation of the circuit:

- *Voltage sensor*: LEM20P. Required for obtaining a measurement of the grid voltage which is necessary for the pPLL to operate and as the sinusoidal reference for the source current to follow.
- *Current sensor*: ACS712. It is needed to measure the source current which is the variable to control by the inner loop of the controller.

For the DSP programming, SolidThinking Embed is suggested in spite of MATLAB/Simulink.

The H-filter has to be retuned in practice depending on the desired performance of the APF.

There are other options to accomplish the task of generating the variable time sampling. It is strongly recommended to try the enhanced capture module (eCAP) of the F28335 DSP which is widely used in systems where the accurate timing is important.

Bibliography

- [1] B. A. Francis and W. M. Wonham, “The internal model principle of control theory,” *Automatica*, vol. 12, no. 5, pp. 457–465, 1976.
- [2] Y. Wang, F. Gao, and F. J. Doyle, “Survey on iterative learning control, repetitive control, and run-to-run control,” 2009.
- [3] Q. Quan and K.-Y. Cai, “A Survey of Repetitive Control for Nonlinear Systems,” *Science Foundation in China*, vol. 18, no. 2, pp. 45–53, 2010.
- [4] K. K. Chew and M. Tomizuka, “Digital Control of Repetitive Errors in Disk Drive Systems,” *IEEE Control Systems Magazine*, vol. 10, no. 1, pp. 16–20, 1990.
- [5] S.-L. Chen and T.-H. Hsieh, “Repetitive control design and implementation for linear motor machine tool,” *International Journal of Machine Tools and Manufacture*, vol. 47, no. 12-13, pp. 1807–1816, 2007.
- [6] J. D. Álvarez, L. J. Yebra, and M. Berenguel, “Repetitive control of tubular heat exchangers,” *Journal of Process Control*, vol. 17, no. 9, pp. 689–701, 2007.
- [7] R. Costa-Castelló, R. Griñó, R. C. Parpal, and E. Fossas, “High-Performance Control of a Single-Phase Shunt Active Filter,” *Ieee Transactions on Control Systems Technology*, vol. 17, no. 6, pp. 1318–1329, 2009.
- [8] R. Costa-Castelló, G. A. Ramos, and J. M. Olm, “Tutorial: Control repetitivo digital de sistemas con frecuencia incierta o variante en el tiempo,” *RIAI - Revista Iberoamericana de Automatica e Informatica Industrial*, vol. 9, no. 3, pp. 219–230, 2012.

- [9] M. Steinbuch, “Repetitive control for systems with uncertain period-time,” *Automatica*, vol. 38, no. 12, pp. 2103–2109, 2002.
- [10] G. A. Ramos, J. M. Olm, and R. Costa-Castelló, “Revisión de control repetitivo digital en condiciones de frecuencia variable,” *Ingeniería e Investigación*, vol. 31, no. 2, pp. 29–37, 2011.
- [11] J. M. Olm, G. A. Ramos, and R. Costa-Castelló, “Adaptive compensation strategy for the tracking/rejection of signals with time-varying frequency in digital repetitive control systems,” *Journal of Process Control*, vol. 20, no. 4, pp. 551–558, 2010.
- [12] C.-L. Chen and Y.-H. Yang, “Spatially Periodic Disturbance Rejection for Uncertain Rotational Motion Systems Using Spatial Domain Adaptive Backstepping Repetitive Control,” *Proceedings of the American Control Conference*, pp. 638–643, 2007.
- [13] Y. H. Yang and C. L. Chen, “Spatially periodic disturbance rejection using spatial-based output feedback adaptive backstepping repetitive control,” *Proceedings of the American Control Conference*, pp. 4117–4122, 2008.
- [14] G. A. Ramos, J. Cortés-Romero, and H. Coral-Enriquez, “Spatial observer-based repetitive controller: An active disturbance rejection approach,” *Control Engineering Practice*, vol. 42, pp. 1–11, 2015.
- [15] B. Singh, K. Al-Haddad, and A. Chandra, “Review of active filters for power quality improvement,” *IEEE Transactions on Industrial Electronics*, vol. 46, no. 5, pp. 960–971, 1999.
- [16] E. Sundaram and M. Venugopal, “On design and implementation of three phase three level shunt active power filter for harmonic reduction using synchronous reference frame theory,” *International Journal of Electrical Power & Energy Systems*, vol. 81, pp. 40–47, 2016.
- [17] P. Zanchetta, M. Sumner, M. Marinelli, and F. Cupertino, “Experimental modeling and control design of shunt active power filters,” *Control Engineering Practice*, vol. 17, no. 10, pp. 1126–1135, 2009.

- [18] A. Poonia and A. Dey, "Space Phasor based Improved Hysteresis Current Controller for Shunt Active Power Filter using 3-Level Inverter," pp. 1–10, 2016.
- [19] K. K. Pedapenki, S. Gupta, and M. K. Pathak, "Comparison of Fuzzy Logic and Neuro Fuzzy Controller for Shunt Active Power Filter," *2015 International Conference on Computational Intelligence and Communication Networks (CICN)*, pp. 1247–1250, 2015.
- [20] T. Wang, J. Fei, and S. Member, "Adaptive Neural Control of Active Power Filter Using Fuzzy Sliding Mode Controller," vol. 4, 2016.
- [21] S. Rahmani, K. Al-Haddad, and H. Y. Kanaan, "A comparative study of shunt hybrid and shunt active power filters for single-phase applications: Simulation and experimental validation," *Mathematics and Computers in Simulation*, vol. 71, no. 4-6, pp. 345–359, 2006.
- [22] W. Shireen and L. Tao, "A DSP-based active power filter for low voltage distribution systems," *Electric Power Systems Research*, vol. 78, no. 9, pp. 1561–1567, 2008.
- [23] G. Mehta, R. D. Patidar, and S. P. Singh, "Design, Analysis and Implementation of DSP based Single-Phase Shunt Active Filter Controller," pp. 1–8, 2011.
- [24] S. Golestan, M. Monfard, F. D. Freijedo, and J. M. Guerrero, "Design and tuning of modified power based PLL for single phase grid connected power conditioning system," *IEEE Trans. Power Electron.*, vol. 27, no. 8, pp. 3639–3650, 2012.
- [25] CENELEC, "En 50160," *European Standard*, pp. 1–20, 2005.
- [26] G. Franklin, J. Powell, and M. Workman, *Digital Control of Dynamic Systems*. Addison-Wesley, third edit ed., 1990.